ACS NANO
Cite This: ACS Nano 2019, 13, 2969–2985
www.acsnano.org

ARTICLE

Protein-Engineered Nanoscale Micelles for Dynamic ^{19}F Magnetic Resonance and Therapeutic Drug Delivery

Lindsay K. Hill,[†,‡,§,¶,○] Joseph A. Frezzo,[†,○] Priya Katyal,[†] Dung Minh Hoang,[‡,§] Zakia Ben Youss Gironda,[‡,§] Cynthia Xu,[†] Xuan Xie,[†] Erika Delgado-Fukushima,[†] Youssef Z. Wadghiri,*[,‡,§] and Jin Kim Montclare*[,†,§,∥,⊥]

[†]Department of Chemical and Biomolecular Engineering, New York University Tandon School of Engineering, Brooklyn, New York 11201, United States

[‡]Center for Advanced Imaging Innovation and Research (CAI^{2}R), New York University School of Medicine, New York, New York 10016, United States

[§]Bernard and Irene Schwartz Center for Biomedical Imaging, Department of Radiology, New York University School of Medicine, New York, New York 10016, United States

[¶]Department of Biomedical Engineering, SUNY Downstate Medical Center, Brooklyn, New York 11203, United States

[∥]Department of Chemistry, New York University, New York, New York 10012, United States

[⊥]Department of Biomaterials, New York University College of Dentistry, New York, New York 10010, United States

Supporting Information

ABSTRACT: Engineered proteins provide an interesting template for designing fluorine-19 (^{19}F) magnetic resonance imaging (MRI) contrast agents, yet progress has been hindered by the unpredictable relaxation properties of fluorine. Herein, we present the biosynthesis of a protein block copolymer, termed "fluorinated thermoresponsive assembled protein" (F-TRAP), which assembles into a monodisperse nanoscale micelle with interesting ^{19}F NMR properties and the ability to encapsulate and release small therapeutic molecules, imparting potential as a diagnostic and therapeutic (theranostic) agent. The assembly of the F-TRAP micelle, composed of a coiled-coil pentamer corona and a hydrophobic, thermoresponsive elastin-like polypeptide core, results in a drastic depression in spin−spin relaxation (T_2) times and unaffected spin−lattice relaxation (T_1) times. The nearly unchanging T_1 relaxation rates and linearly dependent T_2 relaxation rates have allowed for detection *via* zero echo time ^{19}F MRI, and the *in vivo* MR potential has been preliminarily explored using ^{19}F magnetic resonance spectroscopy (MRS). This fluorinated micelle has also demonstrated the ability to encapsulate the small-molecule chemotherapeutic doxorubicin and release its cargo in a thermoresponsive manner owing to its inherent stimuli-responsive properties, presenting an interesting avenue for the development of thermoresponsive ^{19}F MRI/MRS-traceable theranostic agents.

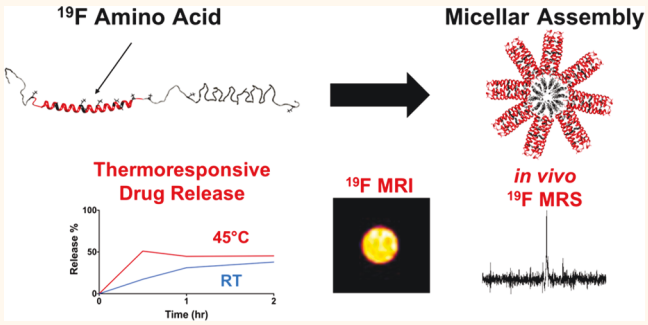

KEYWORDS: *protein engineering, micelle, ^{19}F MRI, self-assembly, theranostic, drug delivery, thermoresponsiveness*

Successful production of a protein-based magnetic resonance imaging (MRI) contrast agent is a challenging yet worthy endeavor,[1−3] as proteins possess malleable architectures and functionalities[4−13] not yet achievable with synthetic materials. Prior attempts of imaging proteins have focused on exploiting the relatively inert properties of serum proteins such as albumin[3] or metal-binding proteins[1,2] that are modified by appending paramagnetic metals (Gd^{3+}, Mn^{2+}) or manipulating superparamagnetic metals (iron oxide) in order to reduce the proton nuclei (^{1}H) spin−lattice (T_1) or spin−spin (T_2) relaxation times, respectively. Reduction in T_1 relaxation times enables high-intensity image acquisition, while a decrease in T_2 relaxation times produces negative contrast images against a high-intensity background.[1,2] Another method for imaging proteins *via* MRI hinges upon

Received: October 1, 2018
Accepted: February 13, 2019
Published: February 13, 2019

DOI: 10.1021/acsnano.8b07481
ACS Nano 2019, 13, 2969–2985

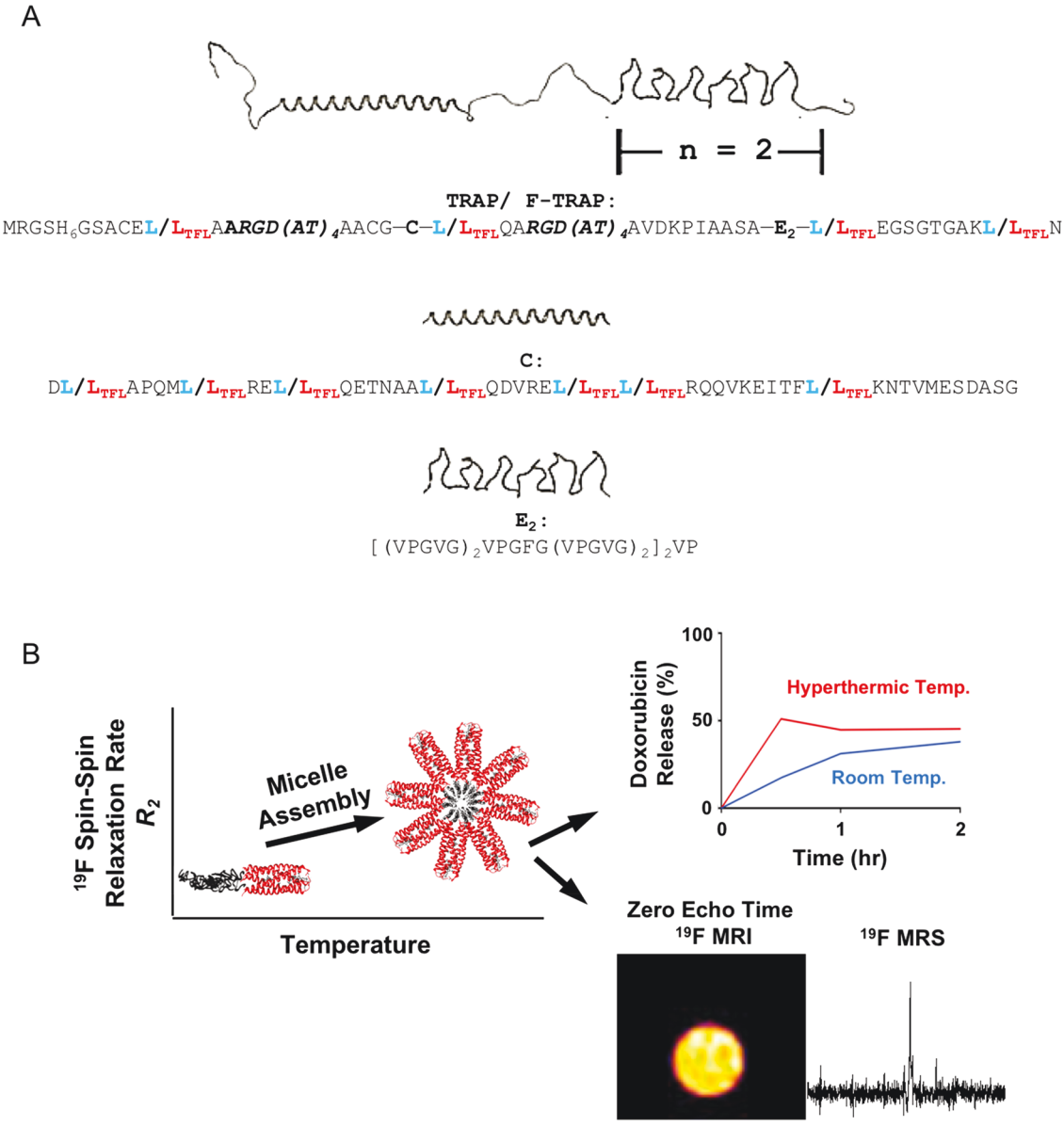

Figure 1. (A) TRAP monomer and sequence showing the coiled-coil (C) domain and elastin-like polypeptide (E) domain. F-TRAP results in replacement of leucine (L, blue) with trifluoroleucine (TFL, red). (B) Schematic representation of F-TRAP assembly, thermoresponsive drug release, and detection by ^{19}F MRS and by zero-echo time (ZTE) ^{19}F MRI when sufficient fluorine is present.

lysine-rich and/or arginine-rich proteins and peptides that contribute exchangeable protons with surrounding water molecules for altering ^{1}H signal in a technique called chemical exchange saturation transfer (CEST).[14] To date, protein and peptide imaging *via* MRI has largely required either chemical modification post-biosynthesis or indirect environmental imaging methods.[15−20]

One alternative technique for imaging proteins is the introduction of fluorine nuclei (^{19}F). The ^{19}F nucleus remains a standard NMR probe because it serves as a steric replacement for hydrogen. In recent years, however, ^{19}F nanoprobes have been exploited for ^{19}F MRI and magnetic resonance spectroscopy (MRS) as an alternative to ^{1}H MRI. This application of ^{19}F is made possible as it exists in 100% natural abundance and elicits a sensitivity of 83% compared to hydrogen,[21−24] yet it is nearly absent in organisms, with the exception of trace amounts found in bone and teeth.[21,25] Therefore, ^{19}F is often pursued as an MRI contrast agent, providing agent-specific signal that can be easily co-registered with a ^{1}H anatomical background.[26−29] While the signal-to-noise (SNR) ratio of ^{19}F MR is not as strong as that of ^{1}H studies, this drawback is mitigated by the lack of background signal in ^{19}F MRI/MRS such that the signal is directly proportional to the concentration of the introduced ^{19}F agent.[30,31]

^{19}F MRI and MRS have been used for a variety of biomedical applications including tumor imaging[32−36] and measuring tumor cell proliferation,[37] cell tracking,[30,38,39] assessing physiological oxygen tension[40] and inflammation,[31] detecting venous thrombosis,[41] and monitoring enzyme activity.[42−45] Recently developed ^{19}F agents take the form of perfluorocarbon nanoemulsions,[36,38,40,41] perfluoropolyethers,[30,33,39,46] polymer-[35,47] and peptide-based nanoprobes,[44] small molecular weight ligands[31] and substrates,[37,43] lipid nanoemulsions,[34] liposomes,[48] metal organic frameworks,[32] nanogels,[49] nanocrystals,[50] and dendrimers.[45] ^{19}F-

DOI: 10.1021/acsnano.8b07481
ACS Nano 2019, 13, 2969−2985

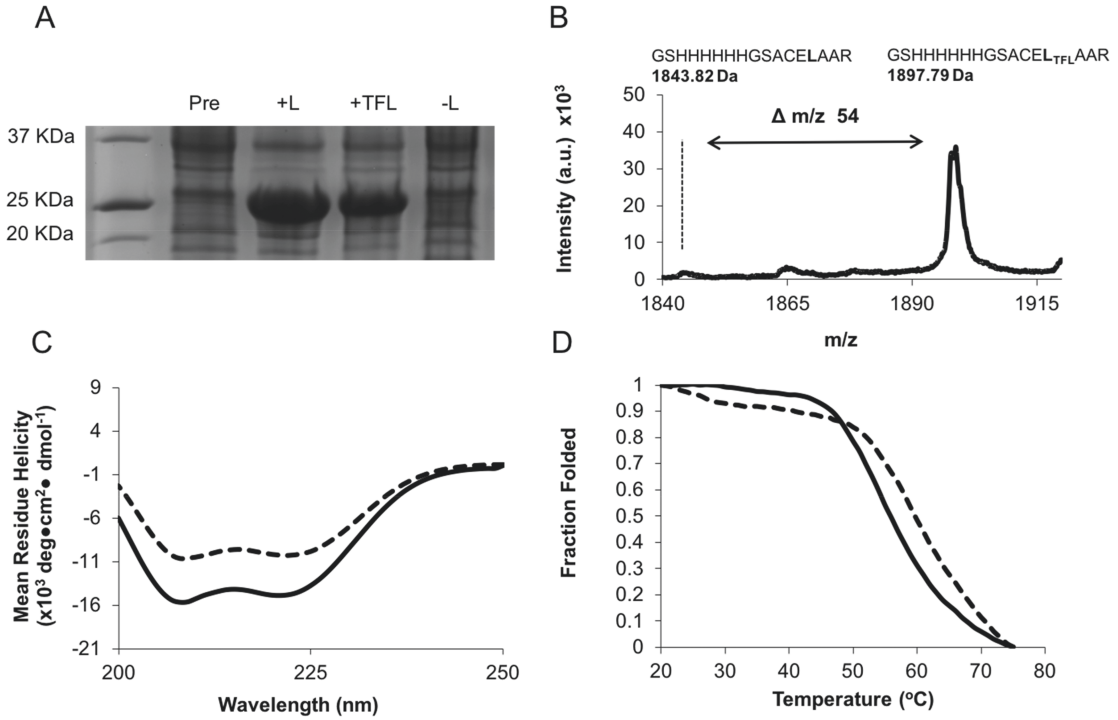

Figure 2. (A) SDS-PAGE of TRAP and F-TRAP overexpression in the presence and absence of L (leucine) or TFL (trifluoroleucine). (B) MALDI-TOF spectrum of tryptic fragment GSHHHHHHGSACEL$_{TFL}$AAR showing a 54 Da mass shift compared to wild-type TRAP. (C) Circular dichroism spectra of TRAP (solid line) and F-TRAP (dashed line) at 0.2 mg/mL and 20 °C. (D) Melt curves for TRAP (solid line) and F-TRAP (dashed line).

incorporated peptides and proteins have also been explored, but to date have only been studied using NMR and phantom MRI.[42,51−55] Solid-phase synthesis of peptides has been used to incorporate fluorinated amino acids;[51] however, this technique can be limited by low yield with increasing peptide chain length.[56] Structural biologists and protein chemists have also biosynthetically incorporated ^{19}F nuclei into proteins, either site-specifically[52] or residue-specifically,[42,53,57] for use as NMR probes to understand structure−function relationships involved in ligand binding[53] and protein folding.[58]

Direct MR visualization of ^{19}F nuclei in proteins is often hindered by unfavorable relaxation properties, which necessitate the inclusion of high concentrations of magnetically equivalent ^{19}F nuclei, long imaging times, and/or chemical conjugation of lanthanide chelates to shorten relaxation times.[25] As the incorporation of fluorinated amino acids can impart benefits to the native protein function, direct imaging of ^{19}F nuclei alone, unadulterated by synthetic linkers or metals, would be an advantageous development for multifunctional imaging agents.

Here we describe the biosynthesis and characterization of a protein block copolymer, or fluorinated thermoresponsive assembled protein (F-TRAP) (Figure 1A), composed of a coiled−coil domain and two repeats of elastin-like polypeptide domains. When subjected to concentration and temperature increases, this construct assembles into nanoscale micelles characterized by a drastic decrease in ^{19}F T_2 relaxation times and nearly constant ^{19}F T_1 relaxation times. The precipitous decrease in ^{19}F T_2 relaxation times results from micelle assembly where NMR-active nuclei in the corona become more ordered and structurally constricted. Here, we overcome the signal loss associated with the dynamic T_2 relaxation properties using a zero echo time (ZTE) ^{19}F MRI pulse sequence, demonstrating the direct imaging of fluorinated amino acids within a protein (Figure 1B) without the aid of lanthanide chelates.[59,60] Furthermore, as a proof-of-concept, this agent was introduced intratumorally into a mouse xenograft model of human breast cancer, enabling the acquisition of an agent-specific ^{19}F MRS signal (Figure 1B) and demonstrating that the agent is detectable *in vivo*.

In addition to ^{19}F MRI/MRS detection, the inclusion of therapeutic capability with diagnostic visualization (Figure 1B) has led to the generation of a dual-purpose theranostic agent.[61] Previous work has shown that the coiled-coil domain of our protein copolymer can bind an array of small molecules within its hydrophobic pore.[5−7,62−66] This pore, along with the hydrophobic core of the assembled micelle, plays a role in binding doxorubicin (Dox), an anthracycline-class chemotherapeutic agent that has broad therapeutic efficacy against an array of tumor types.[67] However, Dox also maintains profound off-target effects,[68] spurring the need for research into Dox-carrying vehicles that provide controlled release.[69−73] We anticipate that this work will encourage additional use of rational design principles in protein engineering to further exploit self-assembly for the controlled release of small-molecule therapeutics and the modification of relaxation properties in ^{19}F MRI/MRS.

RESULTS AND DISCUSSION

Rationale and Protein Synthesis. We have designed TRAP and F-TRAP to contain an N-terminal hexahistidine tag for purification purposes followed by an RGD motif present within an ARGD(AT)$_6$ linker, a modified cartilage oligomeric matrix protein coiled-coil (C) domain,[63] another ARGD(AT)$_6$ linker, and an elastin-like polypeptide (E) region.[5−7] While TRAP is a nonfluorinated protein, F-TRAP bears 5,5,5-DL-

DOI: 10.1021/acsnano.8b07481
ACS Nano 2019, 13, 2969−2985

Table 1. Fluorescence Anisotropy and Static Light Scattering Data for F-TRAP and TRAP

protein	CMC[a] (μM)	mol wt[b] (KDa)	N_{agg}[c] (monomer)	N_{agg}[c] (pentamer)
F-TRAP	0.59 ± 0.02	717.09 ± 22.77	42.43 ± 1.34	8.48 ± 0.26
TRAP	0.75 ± 0.11	682.42 ± 4.77	42.12 ± 0.55	8.42 ± 0.11

[a]Critical micelle concentration. [b]Data determined from Debye plot fit. [c]Aggregation number.

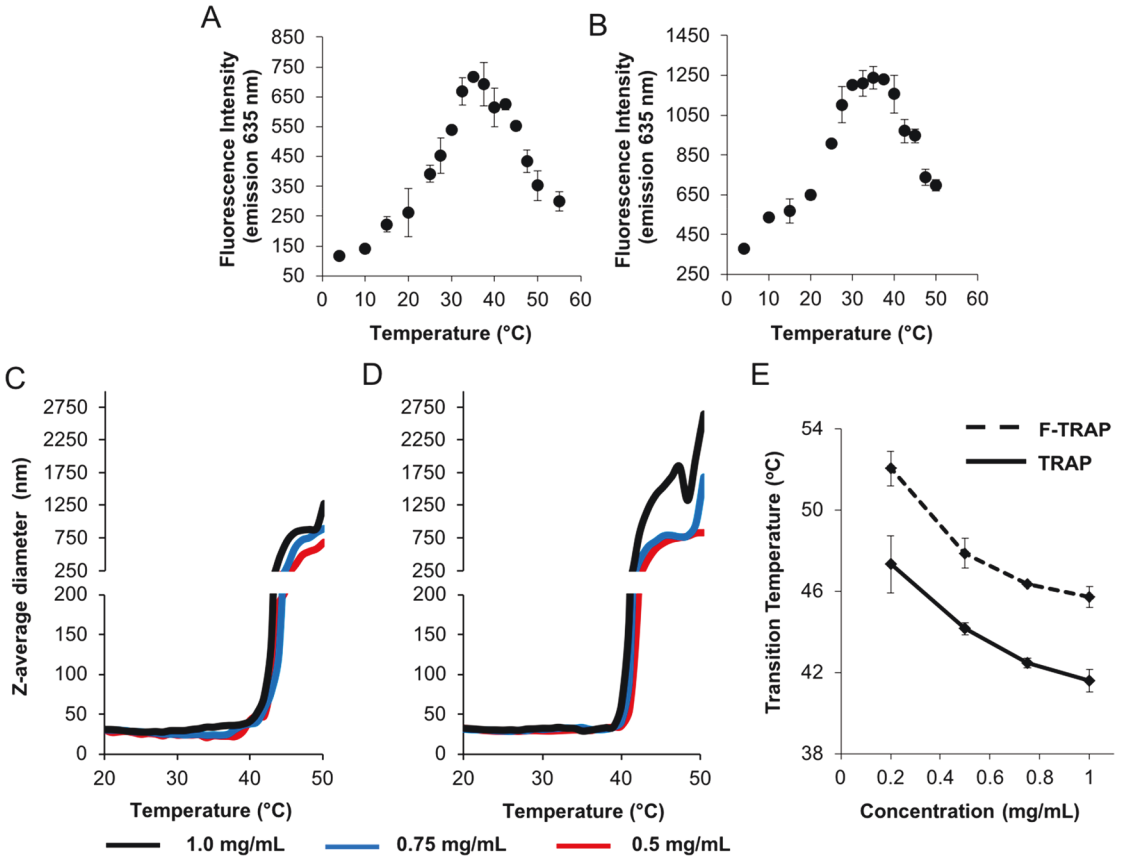

Figure 3. Micelle stability of (A) F-TRAP and (B) TRAP plotted as a function of temperature and Nile red probe fluorescence. Particle diameters of (C) F-TRAP and (D) TRAP by dynamic light scattering at different concentrations and increasing temperature. (E) Inverse transition temperatures (T_t) of F-TRAP (dashed line) and TRAP (solid line) at different concentrations. Error bars represent the standard deviation of three trials.

trifluoroleucines (TFLs), provided during protein expression as a racemic mixture of the two diastereoisomers (2*S*,4*S*)-5,5,5-trifluoroleucine and (2*S*,4*R*)-5,5,5-trifluoroleucine.[4,8−12] The C domain is known to self-assemble into a parallel coiled-coil pentamer,[11] while the E domain, composed of a $[(VPGVG)_2VPGFG(VPGVG)_2]_2$ repeat,[5−7] exhibits an inverse transition temperature (T_t) characterized by a random coil-to-β-spiral conformational change and subsequent chain association dependent on sequence composition.[5−7,74−76]

The TRAP plasmid construct was transformed into the leucine auxotrophic *E. coli* strain LAM1000 for recombinant expression and integration of TFL[4,8−12] to generate F-TRAP (Figures 2A, S1, Table S1). Purified F-TRAP (Figure S1) was assessed for TFL incorporation using matrix-assisted laser desorption ionization-time-of-flight mass spectrometry (MALDI-TOF MS) and amino acid analysis (AAA) (Figures 2B, S2, and S3, Table S2). MALDI-TOF MS and AAA confirmed TFL incorporation of 80.90 ± 1.02% and 81.36 ± 5.22%, respectively (Table S2).

Secondary Structure and Thermostability. Circular dichroism (CD) spectra acquired at 20 °C revealed a 30% loss in negative signal in F-TRAP by comparing the mean residue ellipticity values at 222 and 208 nm to TRAP (Figure 2C, Table S3). Moreover, F-TRAP (T_m = 59.3 ± 2.3 °C) possessed a 5.3 °C higher melting temperature than TRAP (T_m = 54.0 ± 2.0 °C), presumably due to the increased hydrophobicity of TFL[9] (Figure 2D, Table S4). The K2D3 CD deconvolution software[77] corroborated the differences in α-helicity at 20 °C and demonstrated an inversely proportional relationship between α-helical content and β-strand content as a function of temperature. This structural change was an expected result based on the T_t properties of the E domain[6] (Figure S4).

Micellar Assembly and Stability. A highly specific probe, 5-dodecanoyl amino fluorescein (5-daf), was used in fluorescence anisotropy experiments to accurately assess the critical micelle concentration (CMC).[78,79] The 5-daf probe has two functional moieties: (i) a solvatochromic fluorescent component activated in the nonpolar micelle core and (ii) a long saturated aliphatic hydrocarbon chain that inserts slightly into the micelle corona.[78] CMC experiments using 5-daf revealed CMC values of 0.59 ± 0.02 μM and 0.75 ± 0.11 μM for F-TRAP and TRAP, respectively (Table 1). The lower

DOI: 10.1021/acsnano.8b07481
ACS Nano 2019, 13, 2969−2985

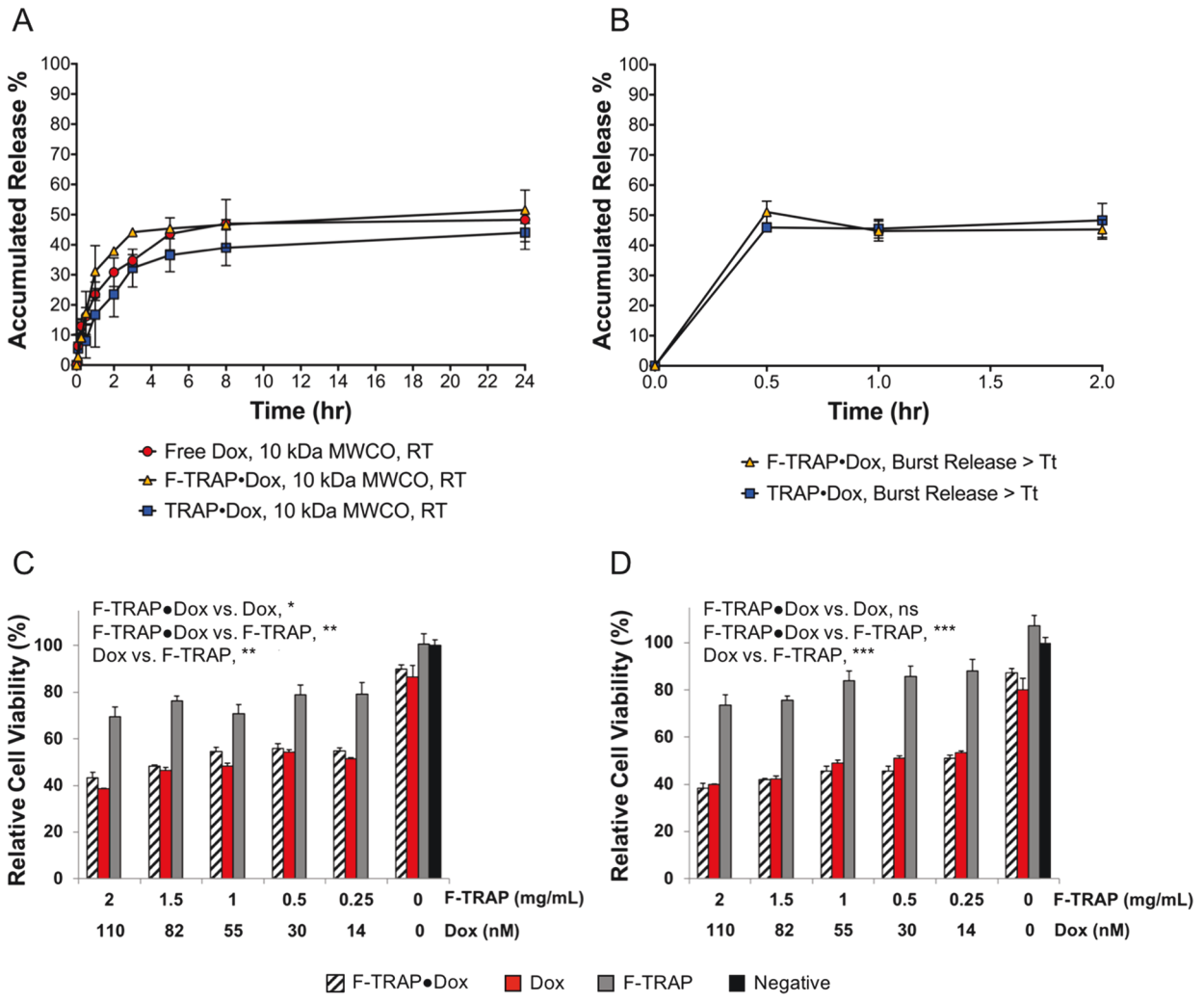

Figure 4. (A) Passive release of free base doxorubicin (Dox) at room temperature (RT) compared to F-TRAP- or TRAP-encapsulated Dox through 10 kDa MWCO dialysis membranes over 24 h. (B) Burst release for Dox from F-TRAP and TRAP at 45 °C (>T_t) over 2 h. MTT cell viability assay for F-TRAP·Dox, Dox alone, or F-TRAP alone at (C) 37 °C or (D) subjected to a 42 °C hyperthermic incubation prior to 37 °C. Symbols in panels C and D indicate the results of Tukey's HSD test for multiple comparisons, applied to assess the significance between treatments on cell viability at each temperature over the range of concentrations studied, where ns = no significance, *$p < 0.05$, **$p < 0.01$, and ***$p < 0.001$. The test also assessed the significance of temperature on Dox and F-TRAP·Dox at 37 °C *vs* 42 °C, where Dox 37 °C *vs* Dox 42 °C = ns and F-TRAP·Dox 37 °C *vs* F-TRAP·Dox 42 °C = *.

CMC value for F-TRAP could be indicative of either a more cooperative assembly of fluorinated protein-based micelles, a result shown in synthetic fluorinated micelles,[80] or simply a probe-specific effect where the long aliphatic hydrocarbon tail of 5-daf fit tightly into the more hydrophobic fluorinated pore of F-TRAP.

We further studied the assembly and stability of F-TRAP and TRAP as a function of temperature (Figure 3A,B) using the small molecular weight solvatochromic probe Nile red.[81] Nile red demonstrates negligible fluorescence in aqueous solution, but shows increased fluorescence when bound within an assembling micellar core.[81−83] An increase in fluorescence intensity was observed at 20 °C with the maximum fluorescence intensity at approximately 35 °C, followed by an emission decrease as the T_t was approached (Figure 3A,B). The increased fluorescent signal up to 35 °C was indicative of increased micelle assembly and, therefore, optimal Nile red uptake, while the subsequent signal decrease suggested micelle disassembly at higher temperatures (Figure 3A,B). Debye plots generated from static light scattering experiments revealed macromolecular F-TRAP assemblies measured at 717.09 ± 22.77 kDa, corresponding to 42.43 ± 1.34 monomeric units or 8.48 ± 0.26 pentameric units (Table 1). TRAP possessed a molecular weight of 682.42 ± 4.77 kDa and showed a similar monomer aggregation number of 42.12 ± 0.55 units and 8.42 ± 0.11 pentamer units (Table 1).

The supramolecular assembly of the proteins was further assessed by dynamic light scattering (DLS) and UV−vis turbidometry analyses with particle morphologies confirmed by transmission electron microscopy (TEM) (Figures 3, S5, S6, S7, Tables S5, S6, S7, S8). As expected,[7] at 20 °C, 0.5 mg/mL F-TRAP assembled into nanoparticles 30.30 ± 0.60 nm in diameter as assessed by DLS, and spherical particles 33.78 ± 6.06 nm in diameter were observed *via* TEM (Figures 3C, S5, S6A, Tables S5, S7). At the same temperature, 0.5 mg/mL TRAP demonstrated slightly larger nanoparticles by DLS (32.14 ± 1.20 nm) with TEM results showing spherical particles of similar size to F-TRAP (34.96 ± 7.30 nm) (Figures 3D, S5, S6C, Tables S6, S8). Increasing F-TRAP and TRAP concentrations, to 0.75 and 1.0 mg/mL, showed a negligible

DOI: 10.1021/acsnano.8b07481
ACS Nano 2019, 13, 2969−2985

difference in size *via* DLS at 20 °C (Tables S5, S6). As the temperature was increased to 50 °C, a dramatic change in size was observed by DLS with near-micrometer size aggregates of F-TRAP (952.06 ± 300.17 nm) and TRAP (1715.96 ± 912.70 nm) at concentrations ranging from 0.5 to 1.0 mg/mL (Figures 3C,D, Tables S5, S6). Proteins prepared at 0.5 mg/mL and 50 °C revealed aggregates on TEM similar in size to those observed by DLS, but with larger polydispersity (724.67−3057.73 nm) (Figure S6B,D, Tables S7, S8).[84,85] The large aggregate size range was reflective of the stochastic nature of the coacervation. The T_t was known to decrease with increasing concentration,[74,76] and here we observed this trend in both F-TRAP and TRAP, with fluorination imparting resistance to coacervation as the T_t was raised by 4.10 ± 0.43 °C (Figure 3E).

DLS was also employed to assess the *z*-average diameters of F-TRAP and TRAP over 24 h at both 35 °C, the temperature at which Nile red fluorescence studies revealed peak micelle formation (Figure S7A,B), and the hyperthermic temperature 42 °C[86] (Figure S7C,D). Upon reaching 35 °C, F-TRAP and TRAP demonstrated similar *z*-average diameters among all three concentrations studied from 0.5 to 1.0 mg/mL with 28.64 ± 2.46 nm for F-TRAP (Figure S7A) and 24.19 ± 4.49 nm for TRAP (Figure S7B). At 35 °C held over 24 h, both F-TRAP and TRAP showed no statistically significant change in *z*-average diameter according to a paired two-tailed Student's *t*-test between 0 and 24 h. These results suggest micelle stability of at least 24 h at 35 °C for both protein assemblies. By contrast, at 42 °C, both F-TRAP (Figure S7C) and TRAP (Figure S7D) exhibited an increase in size. The size of detectable protein aggregates peaked within the first 4 h at 42 °C for 0.75 and 1.0 mg/mL F-TRAP and then drastically reduced as aggregates precipitated out of solution. F-TRAP at 0.5 mg/mL, however, showed peak aggregation size after approximately 8 h at 42 °C before precipitating. TRAP samples showed peak aggregation at 8 h for all concentrations, with 0.75 and 1.0 mg/mL samples subsequently precipitating out of solution, while 0.5 mg/mL remained as large detectable aggregates. These time course studies suggested that F-TRAP and TRAP micelle assemblies were stable for at least 24 h under physiological conditions and again confirmed their capacity for temperature-stimulated coacervation at 42 °C.

Doxorubicin Encapsulation and Thermoresponsive Release. On the basis of previous work, we hypothesized that the C domain of F-TRAP and TRAP would serve as a depot for binding and delivering small molecules.[62,63,66,87] Here, we explored the binding capacity of F-TRAP and TRAP assemblies for Dox, aimed at controlling its release through thermosensitive coacervation of the protein. A 2:1 ratio of Dox:protein was used, and free Dox was removed by size exclusion chromatography (SEC). F-TRAP encapsulated 175% more Dox than TRAP (Table S9). In addition, comparison of the weighted Dox loading revealed 55% greater loading by F-TRAP compared to TRAP (Table S9), likely due to the increased hydrophobicity of the coiled-coil pore of F-TRAP upon incorporation of TFL.

As both F-TRAP and TRAP were capable of binding Dox, we assessed the drug-carrying capabilities of these constructs. Initial experiments quantified the passive release of free Dox or Dox encapsulated by F-TRAP or TRAP at their corresponding loading efficiencies (Table S9) through a 10 kDa MWCO dialysis membrane at room temperature over 24 h (Figure 4A). The dialysis buffer was replaced every 1 h for up to 8 h to prevent the Dox concentration from reaching an equilibrium state. A slow release of Dox through the membrane was exhibited by free Dox, F-TRAP·Dox, and TRAP·Dox with 46.99 ± 7.99%, 46.68 ± 1.67%, and 38.99 ± 5.99% of Dox being collected at 8 h, respectively (Figure 4A). At 24 h, free Dox, F-TRAP·Dox, and TRAP·Dox had released 48.30 ± 9.83%, 51.58 ± 1.39%, and 44.06 ± 3.04% of the initial Dox concentration, respectively (Figure 4A).

To determine whether an increase in temperature could impact Dox release through thermally induced coacervation of the proteins *in vitro*, F-TRAP·Dox and TRAP·Dox were heated at 45 °C for 30 min, 1 h, or 2 h, and the supernatant was assessed for free Dox. By 30 min, Dox release by F-TRAP and TRAP peaked at 51.07% ± 3.60% and 45.96% ± 0.78%, respectively, without further release after 1−2 h of heating (Figure 4B). Therefore, both proteins demonstrated improved drug release at elevated temperature.

In Vitro* Therapeutic Delivery of Doxorubicin to MCF-7 Breast Adenocarcinoma Cells.** The release of Dox by F-TRAP and its therapeutic efficacy was assessed in mammalian tumor cells. MCF-7 human breast adenocarcinoma cells were subjected to treatment with free and F-TRAP-encapsulated Dox in addition to F-TRAP and buffer-only controls (Figure 4C,D). Treatment effects on cell viability were compared *via* Tukey's honestly significant difference (HSD) test for multiple comparisons. MCF-7 cell viability at 37 °C was significantly reduced by both Dox and F-TRAP·Dox, ranging from 0 to 110 nM Dox, compared to F-TRAP alone (**, $p < 0.01$), but the overall effect of Dox on cell viability was significantly stronger than that of F-TRAP·Dox (*, $p < 0.05$). However, while a thermal onus of 42 °C for 1 h and subsequent incubation at 37 °C for 47 h did not affect cell viability under Dox treatment ($p = 0.72$), the hyperthermic state resulted in significantly reduced cell viability with F-TRAP·Dox treatment compared to F-TRAP·Dox at 37 °C (*, $p < 0.05$). This difference suggested that the therapeutic effect of F-TRAP·Dox could be improved under hyperthermic conditions. Again, both Dox and F-TRAP·Dox were significantly more effective at reducing cell viability than F-TRAP alone (, $p < 0.001$).

^{19}F NMR Detection and Relaxation Analysis. F-TRAP was further investigated as a potential dynamic probe for noninvasive ^{19}F NMR, MRI, and MRS using radiofrequency (RF) probes tuned to a ^{19}F Larmor frequency. The limit of detection (LOD)[88−91] for ^{19}F within F-TRAP was assessed using a 400 MHz (9.4 T) NMR spectrometer, with a spectral resolution of 1.36 Hz/pt (0.004 ppm/pt) (Figure 5A); an example ^{19}F NMR spectrum was displayed at 1.125 mg/mL protein concentration (1.84 mM ^{19}F) (Figure 5B). As demonstrated in the example spectrum (Figure 5B), all F-TRAP NMR spectra revealed three peaks spread over approximately 0.6 ppm. The main resonance peak, detected at 3.05 ppm, made up 82.19% of the signal contributed by the three peaks. A second peak, observed at 3.40 ppm, contributed 12.07% of the overall signal, and a third peak, at 3.65 ppm, contributed 5.74% of the signal. The SNRs of the main resonance peak at 3.05 ppm were calculated using the Bruker SINO command at ^{19}F concentrations of 2.5 mM and lower until an SNR = 3 was reached, indicative of the LOD[88] (Figure 5A). The LOD of F-TRAP at 400 MHz, acquired over 264 scans in 3 min 13 s, was reached at 0.25 mM ^{19}F concentration (corresponding to 0.15 mg/mL protein), while the LOD of a commercially available perfluorocarbon nanoemulsion, V-Sense (Celsense), measured using its main resonance peak

DOI: 10.1021/acsnano.8b07481
ACS Nano 2019, 13, 2969−2985

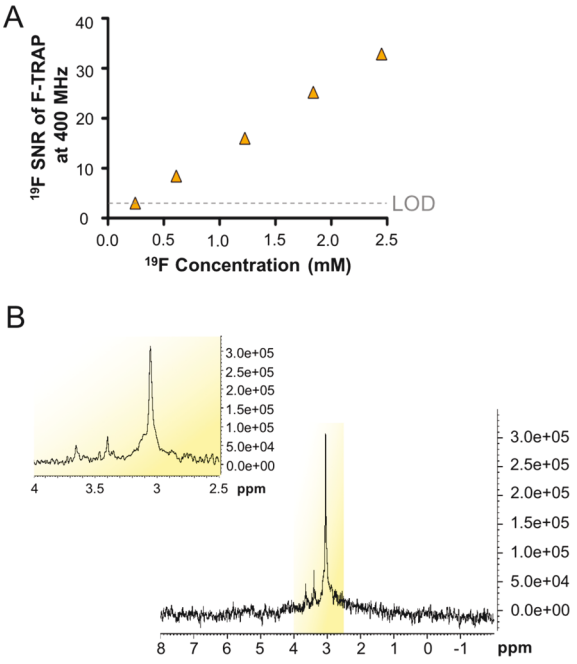

Figure 5. (A) Signal-to-noise ratios (SNR) from 400 MHz one-dimensional ^{19}F NMR spectra acquired over 264 scans in 3 min 13 s for F-TRAP diluted from 2.5 mM ^{19}F to its limit of detection (LOD), at which SNR = 3,[88] of 0.25 mM ^{19}F. (B) Representative 400 MHz one-dimensional ^{19}F NMR spectra of F-TRAP at 1.125 mg/mL protein (1.84 mM ^{19}F), with the inset focused on the three peaks of the F-TRAP spectrum.

detected at −15.04 ppm, was found to be 100-fold lower than that of F-TRAP (Figure S8) at a concentration of 0.0025 mM ^{19}F. Furthermore, the full width of the main resonance peak at half-maximum (fwhm) for F-TRAP and V-Sense were compared at 0.75 mM ^{19}F concentration and found to be 21.14 Hz (0.056 ppm) and 31.60 Hz (0.084 ppm), respectively.

^{19}F NMR spectra of F-TRAP at 1 mg/mL protein concentration (1.63 mM ^{19}F) were then further explored at temperatures of 26.85, 31.85, and 37.0 °C and magnified within a 2 ppm range to compare the F-TRAP peaks (Figure S9). The main resonance peaks demonstrated a minor chemical shift of 0.03 ppm with increasing temperatures, resonating at 3.87, 3.88, and 3.90 ppm for 26.85, 31.85, and 37.0 °C, respectively.

The longitudinal ($R_1 = 1/T_1$) and transverse ($R_2 = 1/T_2$) relaxation times of F-TRAP were assessed *via* inversion recovery and Carr−Purcell−Meiboom−Gill (CPMG) pulse sequence experiments, respectively, *via* ^{19}F NMR (Figure 6A,B). The relaxation experiments were performed to not only attain a deeper understanding of the macromolecular assembly of F-TRAP, but to also serve as an aid in selecting pulse sequence experiments for acquiring reliable MRI signals. Inversion recovery experiments, performed in predominantly water-based solvent systems, revealed a near-uniform resistance of the longitudinal relaxation rates ($R_1 = 1/T_1$) to both temperature and concentration increases, yielding values in the range of approximately 0.002−0.004^{-1} ms (Figure 6A, Table S10). The ^{19}F spin−spin relaxation times, however, presented an interesting depiction of protein assembly as R_2 ($=1/T_2$) relaxation times increased with restricted motion of nuclei,[92,93] a characteristic observed in synthetic micelles.[92] This assembly-driven restriction of internal ^{19}F atom mobility was further corroborated by the observed increase in R_2/R_1 relaxation rate (Tables S10, S11).[52,92,93] The increase in R_2 relaxation rates illustrated linearity while maintaining the same enhanced sensitivity when reaching the F-TRAP CMC (Figure 6B, Table S11). A thorough quantitative analysis revealed a 17000-fold increase in sensitivity when comparing the r_2/r_1 relaxivity values within the 22−37 °C temperature range (F-TRAP exhibited the following R_1 and R_2 relaxivity ranges [−0.09: −0.03] s^{-1}/°C and [2009.16:17396.80] s^{-1}/°C, respectively). Compared to the consistent temperature-dependent slope, the observed concentration effect is minor within the range of 0.6−0.9 mg/mL F-TRAP concentration (0.98−1.47 mM ^{19}F, respectively) (Figure 6B). This temperature-dependent R_2 increase could be exploited to monitor the accumulation of F-TRAP at a site of interest (*e.g.*, tumor) and its response to external heating.

Phantom ^{19}F MRI Detection. Since R_2 demonstrated a much greater linear dependence on temperature than R_1, F-TRAP was deemed a likely candidate as a T_2-MRI temperature sensor that would require strategies for spatial localization reliant on rapid acquisition of echo-trains and short repetition times in order to generate an appropriate SNR.[94] Given that shortened T_2 times restrict high signal intensity attainment and that imaging is further hampered by low ^{19}F content, we acquired zero-echo time pulse sequence MRI on F-TRAP. ZTE MRI overcomes signal loss as a result of very short T_2 relaxation times[95,96] and is often used for the detection of tendons, cortical bone, and ligaments.[97,98] A homemade whole body birdcage coil was inductively coupled to a slotted resonator for broadband tuning *via* a variable capacitor capable of housing two glass tubes (Figure 6C). Two samples, water as a control for ^{1}H signal and F-TRAP (13.40 mg/mL or 0.82 mM protein, equivalent to 21.90 mM ^{19}F) for the experimental ^{19}F MRI signal, were scanned. The phantom samples for the water and F-TRAP (Figure 6D) both generated a positive signal for ^{1}H nuclei (Figure 6E). The ^{19}F signal from F-TRAP was examined using a ZTE MRI sequence while ensuring that the total imaging time was realistically achievable *in vivo* (in the present case: 1 h) (Figure 6F). In 1 h, ZTE imaging with a spatial resolution of (468 μm)^2 achieved an SNR of 43 (Figure 6F,G). The corresponding limit of detection,[89] at which the SNR = 3, of the ZTE sequence at 7 T under current experimental conditions was measured to be 0.91 mg/mL F-TRAP (1.49 mM ^{19}F). ^{19}F MRS, with a spectral resolution of 97.66 Hz/pt (0.35 ppm/pt), was also performed on the 13.40 mg/mL F-TRAP phantom sample in order to assess the difference in spectrum compared to that achieved *via* ^{19}F NMR (Figure S10). Notably, only one peak was obtained by ^{19}F MRS, in contrast to the three peaks observed on NMR. This F-TRAP peak resonated at 3.11 ppm (Figure S10), showing little shift from the 3.05 ppm main resonance peak observed on NMR (Figure 5B). However, the fwhm of the ^{19}F MRS peak was 540.37 Hz (1.91 ppm), likely broadened by the lower static magnetic field homogeneity inherent to MRI scanners[99] and resulting in a lower spectral resolution requirement. The width of this single peak encompassed the entire 0.6 ppm spread of the three F-TRAP peaks detected *via* ^{19}F NMR.

***In Vivo* Detection in an MCF-7 Xenograft Mouse Model.** Following ultrasound imaging to confirm a tumor size of at least 100 mm^3 in MCF-7 xenograft CrTac:NCr-*Foxn1*^{nu} mice (Figure S11), *in vivo* detection of intratumorally injected near-infrared (NIR) fluorochrome-conjugated F-TRAP (NIR-

DOI: 10.1021/acsnano.8b07481
ACS Nano 2019, 13, 2969−2985

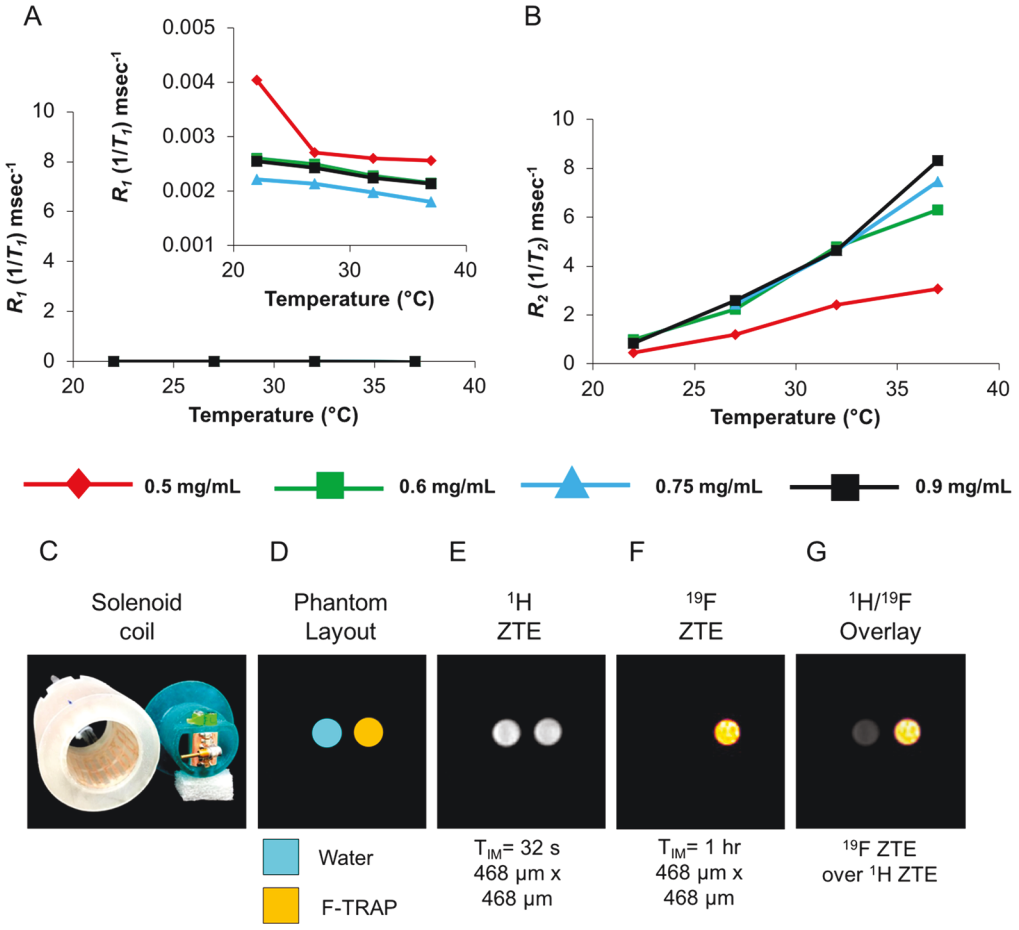

Figure 6. (A) ^{19}F R_1 and (B) ^{19}F R_2 relaxometry plots. Inset in A shows R_1 plot on a smaller scale. (C) Homemade whole body linear birdcage coil (left, in white) inductively coupled with a slotted resonator (right, in blue) capable of holding two glass tubes (o.d. 6 mm) and broadband tuning *via* a variable capacitor. (D) MRI phantom layout, (E) zero echo time (ZTE) imaging of ^{1}H nuclei, (F) ZTE imaging of ^{19}F nuclei, and (G) overlay of ^{1}H and ^{19}F ZTE. T_{IM} = total acquisition time.

F-TRAP) was assessed using fluorescence imaging and ^{19}F MRS (Figure 7). The route of intratumoral injection was chosen as a preliminary assessment of the *in vivo* detection of F-TRAP by ^{19}F MRS because it has previously proven successful for other elastin-like polypeptide-containing constructs, providing retention of the chemotherapeutic at the tumor site with minimal exposure to healthy tissues and is most often used in cases where surgery is not advised or when the tumor size must be reduced prior to surgery.[100−105] Pre-injection fluorescence imaging overlaid onto an anatomical reflectance image revealed baseline fluorescence values that did not exceed 10 picowatts per mm^2 (pW/mm^2) (Figure 7A). Following the injection of 13.40 mg/mL NIR-F-TRAP (equivalent to 0.82 mM F-TRAP and 21.90 mM ^{19}F), tumor fluorescence exhibited an intensity of up to 2.5 × 10^{003} pW/mm^2 (Figure 7B), confirming successful intratumoral injection of NIR-F-TRAP. A 24 h post-injection dual fluorescence-reflectance image of the same subject showed the fluorescence signal had cleared from the tumor, with only a low level (~300 pW/mm^2) of fluorescence visible at the periphery of the tumor (Figure S12). Injected mice were followed for up to 1 week post-injection and showed no signs of acute toxicity.

Immediately following the initial post-injection fluorescence imaging, *in vivo* MR studies were conducted using a house-made setup composed of a ^{19}F-tunable low-pass ladder surface coil inductively coupled to the same homemade whole body coil used for phantom imaging (Figure 7C), which was placed directly over the tumor. A low-resolution (234.375 μm)^3 ^{1}H T_1-weighted 3D fast low-angle shot (FLASH) MRI was used to identify the location of the tumor within the MRI field of view (FOV) and confirm the appropriate time window for ^{19}F MRS acquisition (Figure 7D). The superficial tumor was identified in all three dimensions within the FOV (Figure 7D). *In vivo* ^{19}F MRS, with a spectral resolution of 97.66 Hz/pt (0.35 ppm/pt), was obtained from the entire tissue covered by the surface coil. Similar to the ^{19}F MRS spectrum of the F-TRAP phantom (Figure S10), *in vivo* MRS of NIR-tagged and intratumorally injected NIR-F-TRAP revealed a single ^{19}F peak (Figure 7E). The single peak resonated at 13.50 ppm with an SNR of 11.19 acquired over 200 scans in 6 min 40 s. The fwhm of the peak was 332.00 Hz (1.17 ppm), again encompassing the 0.6 ppm spread of the three F-TRAP peaks detected *via* ^{19}F NMR.

CONCLUSIONS

We present the biosynthesis and characterization of protein-engineered block copolymers that assemble into micelles for ^{19}F MRS and MRI. We employ ZTE MRI, an approach with stringent requirements, but one that enables near spin density images that align with the nanometer-sized micellar assembly properties of F-TRAP. ^{19}F ZTE MRI was utilized as a proof-of-concept imaging sequence to demonstrate the ability to visualize F-TRAP within just 1 h acquisition time at 13.40 mg/

DOI: 10.1021/acsnano.8b07481
ACS Nano 2019, 13, 2969−2985

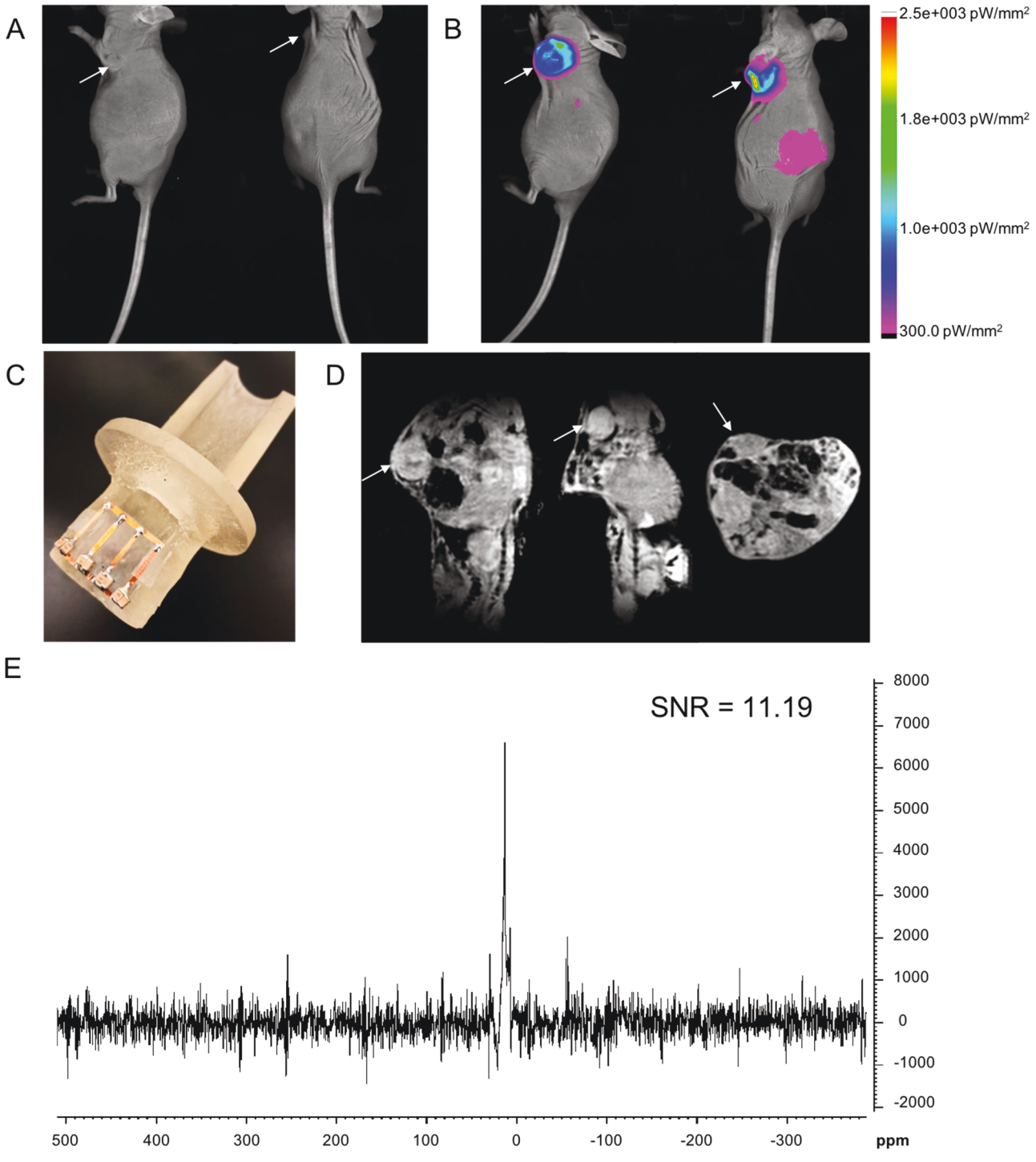

Figure 7. *In vivo* fluorescence-reflectance imaging of MCF-7 xenograft mouse model (A) pre-injection of NIR-F-TRAP and (B) immediately following intratumoral injection of NIR-F-TRAP. (C) Homemade animal holder attached to a ^{19}F-tunable low-pass ladder surface coil for inductive coupling and fitting with the whole body coil described in Figure 6C. (D) Sagittal, coronal, and axial views from a 3D *in vivo* ^{1}H T_1-weighted FLASH MRI of a NIR-F-TRAP-injected mouse with FOV focused around the MCF-7 tumor. (E) *In vivo* ^{19}F MRS, and corresponding SNR, of a NIR-F-TRAP-injected mouse acquired in 6 min 40 s.

mL F-TRAP (0.82 mM F-TRAP, 21.90 mM ^{19}F). ^{19}F MRS was able to detect intratumorally injected F-TRAP signal in a mouse model in under 7 min, allowing for rapid detection and monitoring of the agent *in vivo*. While the F-TRAP monomer bears a measured 26.77 ^{19}F atoms (1136 ^{19}F atoms per micelle), it demonstrates significant signal intensity *via* ZTE MRI despite the R_2 alterations. Improvements in coil design and pulse calibration,[106] or the use of more effective pulse sequence schemes,[95,107] will improve our ability to detect F-TRAP *in vivo* using ^{19}F ZTE MRI, allowing for further exploitation of F-TRAP's temperature-dependent R_2 sensitivity. By measuring the R_2 values, after at least 0.6 mg/mL F-TRAP has accumulated, or the ^{19}F MRS intensity after *in vivo* administration and imaging, we could determine the F-TRAP localization and concentration at specific organ sites. Furthermore, localized heating could increase this R_2 effect,

DOI: 10.1021/acsnano.8b07481
ACS Nano 2019, 13, 2969−2985

creating an on/off MRI switch. This T_2-nanothermometer application is currently being explored, and initial experiments (Figures 6A,B, S13) suggest promise in monitoring F-TRAP's theranostic drug thermorelease function. The theranostic aspect of F-TRAP is apparent when examining its ability to bind Dox, due to both the hydrophobic coiled-coil pore and micellar core, and its effective drug release to MCF-7 breast adenocarcinoma cells particularly under hyperthermic conditions. Promising *in vivo* ^{19}F MRS studies and *in vitro* Dox delivery encourage future *in vivo* dual therapeutic−diagnostic studies under normal physiological and hyperthermic conditions to assess the theranostic potential of F-TRAP, including targeting through its RGD sequences or other tumor-targeting domains, by monitoring its *in vivo* drug release with simultaneous ^{19}F MRI/MRS detection.

In conclusion, this work describes a biosynthesized fluorinated protein for MR detection that does not require post-translational modification. In terms of protein-based MRI contrast agent development, these results provide a template for rationally designing self-assembling biomaterials. The ability to design MR molecular probes at the genetic level allows for construct modification tailored to specific needs, such as targeting sequences unique to a tissue or cell type of interest, sequence mutations that alter the drug-loading capacity of the construct and stimuli-responsive cargo delivery, or an alteration in the number of potential sites for fluorinated residue incorporation.[4−12] Protein engineering, therefore, has great potential in the development of fluorinated theranostic agents.

EXPERIMENTAL SECTION

Materials. PfuUltra HotStart DNA polymerase and 10× PfuUltra HotStart reaction buffer were purchased from Agilent Technologies. DpnI enzyme was purchased from New England BioLabs. The miniprep plasmid purification kit was purchased from Zymogen. Deoxynucleotide triphosphates mix, sodium phosphate dibasic, sodium chloride, urea, imidazole, isopropyl β-D-1-thiogalactopyranoside (IPTG), glucose monohydrate, tryptone, tryptic soy agar, yeast extract, ampicillin, kanamycin, magnesium chloride, calcium chloride, thiamine hydrochloride, HisPur Ni-NTA agarose, tricine, Pierce bicinchoninic acid (BCA) assay kit, Pierce snakeskin dialysis tubing 3.5 kDa molecular weight cut off (MWCO), Pierce high-capacity endotoxin removal spin columns, 5-dodecanoyl amino fluorescein, Vybrant MTT cell viability assay, methanol, and sodium dodecyl sulfate were acquired from Thermo Fisher Scientific. Racemic 5,5,5-trifluoroleucine was purchased from Oakwood Chemical. Nile red, acetonitrile, trifluoroacetic acid, all 20 amino acids, α-cyano-4-hydrocinnamic acid, sequencing grade modified trypsin, Proteomass peptide and protein MALDI-MS calibration kit, and β-estradiol were purchased from Sigma-Aldrich. Formvar square mesh copper TEM grids were purchased from Electron Microscopy Sciences. Macrosep and Microsep advance centrifugal 3 kDa MWCO devices and acrodisc 0.2 μm syringe filters were purchased from Pall. C18 packed zip-tips and Durapore 0.2 μm membrane filters were purchased from EMD Millipore. Acrylamide/bis solution (30%) 29:1, Precision Plus protein dual-color standards, and Gene Pulser electroporation cuvettes were purchased from Bio-Rad. Free base doxorubicin was purchased from MedKoo Sciences. VivoTag-S 750 was purchased from PerkinElmer. Corning Matrigel matrix was purchased from Corning. MCF-7 cells were purchased from ATCC, and CrTac:NCr-*Foxn1*^{nu} nude mice were acquired from Taconic Biosciences.

TRAP and F-TRAP Construction and Production. TRAP is derived from the CE_2 parent construct that was previously generated and thoroughly characterized.[5,6] Two RGD mutations located at sites flanking the C domain were introduced by site-directed mutagenesis in the pQE30/CE_2 plasmid. Mutant constructs were generated by a polymerase chain reaction (PCR) using high-fidelity PfuUltra HotStart Taq polymerase (2.5 units/μL), 10× PfuUltra reaction buffer, deoxynucleotide triphosphates mix (10 mM), and the following primers (125 ng/μL) from MWG Operon: RGDlink1fwd 5′-GAGCTCGCTGCTCGTGGCGACGCCACTGCTACG-3′, RGDlink1rev 5′-CGTAGCAGTGGCGTCGCCACG-AGCAGCGAGCTC-3′, RGDlink2fwd 5′-CTGCAGGCTGCC-CGTGGCGACGCTACTGCAACC-3′, and RGDlink2rev 5′-GGTTGCAGTAGCGTCGCCACGGGCAGCCTGCAG-3′. After PCR, the methylated parent strand was digested for 3 h at 37 °C with DpnI enzyme. The resultant mutant constructs were transformed into chemically competent XL1-Blue *E. coli* cells and permitted to grow on tryptic soy agar plates for approximately 16 h at 37 °C under ampicillin (200 μg/mL) antibiotic selection control. DNA was extracted, and the resulting purified plasmid pQE30/TRAP was confirmed *via* sequencing (Eurofins Operon).

pQE30/TRAP plasmid was transformed into electrocompetent leucine auxotrophic LAM1000 *E. coli* cells,[4,8−10,12] a gift from David Tirrell (California Institute of Technology) and permitted to grow on tryptic soy agar plates for approximately 12 h at 37 °C under both kanamycin (35 μg/mL) and ampicillin (200 μg/mL) antibiotic selection control. Single colonies were selected for growth in starter cultures (5 mL) of minimal media M9 (0.5 M Na_2HPO_4, 0.22 M KH_2PO_4, 0.08 M NaCl, 0.18 M NH_4Cl) in the presence of kanamycin (35 μg/mL), ampicillin (200 μg/mL), vitamin B_1 (35 μg/mL), $MgSO_4$ (100 mM), $CaCl_2$ (0.1 mM), and 20 amino acids (40 μg/mL) for approximately 16 h at 37 °C and 350 rpm. The starter cultures were then transferred to a large-scale expression flask (200 mL for TRAP, 500 mL for F-TRAP) at volumetric percentages of 2% containing the aforementioned M9 media and associated chemicals used for starter culture preparation. The large-scale cultures were grown at 37 °C and 300 rpm until the optical density at 600 nm reached 0.8−1.0. At this step, TRAP expression was induced with the addition of IPTG (200 μg/mL). Following 3 h of protein expression, at 37 °C and 300 rpm, the cells were pelleted by centrifugation at 4000 rpm for 15 min at 4 °C. The cell pellets were stored at −80 °C until purification. For F-TRAP expression, when the optical density at 600 nm reached 0.8−1.0, the cells were pelleted by centrifugation at 4000 rpm for 15 min at 4 °C and washed three times with ice cold 0.9% NaCl. After the final centrifugation, the pellet was resuspended in the aforementioned M9 media with 19 amino acids, minus leucine, and all other associated chemicals. The resuspended cell mixture was permitted to grow for 15 min at 37 °C and 300 rpm to exhaust any additional leucine. Following this growth period, TFL (555 μg/mL) and IPTG (200 μg/mL) were added to induce expression and residue-specific incorporation of TFL.[9,10,108] After 3 h of protein expression at 37 °C and 300 rpm, the cells were pelleted by centrifugation at 4000 rpm for 15 min at 4 °C. The cell pellets were stored at −80 °C until purification.

Cell pellets were permitted to thaw at 4 °C for 30 min and then resuspended in lysis buffer (6 M urea, 50 mM Na_2HPO_4, 0.5 M NaCl, pH 8.0). Lysis was achieved by two freeze−thaw cycles between −80 °C and room temperature followed by ultrasonic probe sonication (Q500 sonicator, amplitude 50%, pulse 5 s on and 30 s off, in an ice water bath for a total sonication time of 1 min and 30 s) until cell lysate was visually transparent. The cell lysate was centrifuged at 13500 rpm for 1 h at 4 °C. The supernatant was then combined with HisPur Ni-NTA agarose slurry, pre-equilibrated with lysis buffer according to the manufacturer's instructions, and left to incubate with end-over-end mixing (Labquake Rotisserie, Barnstead Thermolyne) overnight at 4 °C. The protein of interest was eluted by increasing elution buffer (6 M urea, 50 mM Na_2HPO_4, 1 M imidazole, pH 8.0) with effective imidazole concentrations ranging from 25 to 1000 mM. All fractions were subjected to 12% SDS-PAGE to confirm purity. Pure protein, typically in the elutions spanning 100−1000 mM imidazole, was then dialyzed in snakeskin tubing, 3.5 kDa MWCO, across four buckets (3.5 L each) of 50 mM Na_2HPO_4 and 0.5 M NaCl, pH 8.0 at 4 °C. Following dialysis, the protein was concentrated with a Macrosep Advance centrifugal device (3 kDa MWCO) at 3500 rpm at 4 °C. After 0.2 μm syringe filtration, the

DOI: 10.1021/acsnano.8b07481
ACS Nano 2019, 13, 2969−2985

concentration of each protein was determined by BCA assay. Proteins were stored at 4 °C.

Confirmation of TRAP and F-TRAP Composition. TRAP and F-TRAP samples at effective concentrations of 0.2 mg/mL were subjected to targeted enzymatic digestion with sequencing-grade modified trypsin (0.2 mg/mL, 2% v/v), pre-warmed to 30 °C for 15 min prior to addition, in 60 mM ammonium bicarbonate buffer for 6 h at 37 °C with 300 rpm mixing. Trypsin digestion was quenched with trifluoroacetic acid (TFA) (10% v/v in diH_2O) until the pH reached approximately 4.0. Digested TRAP and F-TRAP were then subjected to zip-tip preparation using C18 packed tips. Tips were wetted in 50% v/v acetonitrile in deionized water (diH_2O) and equilibrated in 0.1% v/v TFA in diH_2O prior to protein binding and subsequent elution from the C18 column with 0.1% v/v TFA in 75% acetonitrile into the saturated α-cyano-4-hydrocinnamic acid matrix at 1:1 protein:matrix volumetric ratio. TRAP and F-TRAP samples were spotted in 1 μL volumes on a MALDI-TOF MS steel target plate and permitted to dry under vacuum for 1 h. A theoretical trypsin digestion of TRAP was performed with the online tool Expasy PeptideMass (http://web.expasy.org/peptidemass/) with adjustments made after theoretical digestion to account for size increase upon TFL substitution at all leucine sites for F-TRAP. The UltrafleXtreme MALDI-TOF (Bruker) was calibrated with the following standards: bradykinin fragment 1−7, angiotensin II, $P_{14}R$ (synthetic peptide), adrenocorticotropic hormone fragment 18−39, insulin chain B oxidized (bovine origin), and insulin (bovine origin), all at working solutions of 10 pmol/μL. Equal volumes of standards were collected in a single tube and combined in a 1:1 volumetric ratio with the α-cyano-4-hydrocinnamic acid matrix. The mass spectra were analyzed for TFL incorporation according to peak intensities. Amino acid analysis was also performed by John Schulze and the team at Molecular Structure Facility (*via* Science Exchange) at University of California, Davis, on the same proteins and analyzed on an L-8800 Hitachi analyzer, utilizing a sodium citrate buffer system.

Secondary Structure and Thermostability Analysis. Circular dichroism spectroscopy was used to assess the secondary structure and thermostability of TRAP and F-TRAP. This was accomplished using a Jasco J-815 CD spectrometer with a PTC-423S single-position Peltier temperature control system. TRAP and F-TRAP proteins were diluted to 10 μM concentrations in 50 mM Na_2HPO_4 and 0.5 M NaCl, pH 8.0, and dispensed into quartz cuvettes. The wavelength spectrum was measured over the range of 200−250 nm with a bandwidth (step size) of 1 nm and path length of 1 cm.[5−7,9] The scanning mode was continuous at 20 nm/min. All wavelength CD runs were conducted in triplicate at 20 °C. Data represent an average of three independent protein preparations. Temperature scans were performed at 222 nm from 20 to 75 °C, at a heating rate of 1 °C/min. The melting temperature (T_m) was determined by taking the first derivative of the normalized mean residue ellipticity as a function of temperature.[5−7] The T_m was confirmed with additional temperature scans using protein concentrations of 5 and 15 μM so as to separate the constant T_m from the dynamic inverse transition temperature (T_t). Using spectral analysis software provided by the instrument manufacturer (Jasco), all spectra underwent a 50 mM Na_2HPO_4/0.5 M NaCl, pH 8.0, buffer spectrum subtraction followed by a smoothing operation according to the Savitzky−Golay method at a convolution width of 21.[109] In terms of calculations for CD analysis, mean residue ellipticity (θ_{MRE}) was calculated from ellipticity (θ) using the following equation:[63]

$$\theta_{MRE} = \theta/(10 \times \text{Protein Conc} \times \text{Path Length} \times \text{Residue Number})$$

Deconvolution of spectra at each temperature, accounting for buffer subtraction, smoothing, and mean residue ellipticity calculations, was carried out using K2D3 software (http://cbdm-01.zdv.uni-mainz.de/~andrade/k2d3//index.html) to determine the α-helix and β-strand composition.[77]

Turbidometry and Inverse Transition Temperature Analysis. TRAP and F-TRAP at varying concentrations were loaded into a type 21 quartz cuvette with a 10 mm path length (BuckScience). Proteins were characterized for their inverse transition temperature (T_t) behavior at 320 nm using a UV−vis Cary-50 (Varian Inc.) equipped with a TC125 temperature regulator (Quantum Northwest). Samples were heated at a rate of 1 °C/min from 20 to 80 °C. The T_t was determined by taking the first derivative of the normalized absorbance at 320 nm as a function of temperature. At least three separate protein preparations were subjected to UV−vis spectroscopy across all concentrations.

Self-Assembly and Analysis. Fluorescence anisotropy experiments were carried out on a Molecular Devices Flexstation 3 plate reader equipped with the necessary hardware for fluorescence polarization measurements. 5-Dodecanoyl amino fluorescein (10 nM) dissolved in methanol was added to clear glass threaded vials and dried to a thin film under vacuum. Protein was then added to each tube at increasing concentrations, and the tubes were sealed tightly and gently agitated (80 rpm orbital mixing) at 25 °C for 24 h before measuring the fluorescence polarization (excitation 485 nm, emission 528 nm, cutoff 515 nm, *G* factor 1.0). The critical micelle concentration was determined to be the concentration at which fluorescence polarization increased dramatically.[78] These experiments were conducted at least three times with two different protein preparations with the average CMC taken for all trials.

Fluorescence experiments were carried out to measure micelle stability as a function of temperature using a Biotek Synergy HT plate reader. Nile red (1 μM) dissolved in methanol was added to PCR tubes and dried to a thin film under vacuum. Protein was added to each tube at a static concentration of 0.5 mg/mL at 4 °C. Tubes were quickly transferred to a Bio-Rad thermocycler and then slowly heated (0.1 °C/s) with 10 min incubation periods at each measured temperature. At the conclusion of each incubation period, the contents of each tube were subjected to fluorescence measurements (excitation 550 nm, emission 635 nm). These experiments were conducted at least three times with two different protein preparations.

Static light scattering experiments were carried out using a Zetasizer Nano Series model Nano ZS90 (Malvern Instruments). Proteins ranging in concentration from 0.25 to 2.0 mg/mL were incubated at 35 °C for 24 h with mild agitation (80 rpm orbital mixing). After 24 h, the tubes were visually inspected for aggregation, and after confirming that coacervation had not occurred, the protein molecular weights were measured using Debye plot fitting of KC/R_θ (where K is the Debye constant, C is the concentration, and R_θ is the Rayleigh ratio) plotted against the concentration. The y intercept was determined to be the molecular weight.[110] These experiments were conducted at least three times with two different protein preparations with the average molecular weights taken for all trials.

Dynamic light scattering measurements were performed on a Zetasizer ZS90 in a low-volume disposable cuvette with the applied settings: material protein (refractive index 1.450), absorption 0.001, dispersant phosphate buffer with a viscosity of 1.0200 cP, and refractive index of 1.335. Approximately 1.0 mL of 0.5, 0.75, or 1.0 mg/mL TRAP or F-TRAP in 50 mM Na_2HPO_4/0.5 M NaCl, pH 8.0, was double filtered (0.2 μm) to minimize contamination and then added to the cuvette for analysis. Three separate protein preparations were subjected to DLS measurements, and the average z-average diameters among the trials were plotted. To assess the effect of temperature on protein assembly, three independent measurements were taken, conducting 10 runs for each measurement (5 s per run), with a delay time of 2 s from 20 to 50 °C. Stability of the protein assembly was also investigated *via* DLS using the above parameters to measure the z-average diameters from 20 °C to either 35 or 42 °C, at which point measurements were taken every 30 min for 12 h and, subsequently, every 1 h through 24 h.

TEM experiments were undertaken to visualize and confirm particle assembly and sizes. The TRAP and F-TRAP proteins (0.5 mg/mL) were heated to 20 or 50 °C for 1.5 h followed by a 2 μL application of the protein onto a 400 square mesh copper TEM grid for 30 s. Excess protein was blotted from the grid with filter paper and then subjected to two washes with diH_2O. Uranyl acetate (1% w/v) in a 1 μL volume was applied to the grid, quickly blotted, and followed

DOI: 10.1021/acsnano.8b07481
ACS Nano 2019, 13, 2969−2985

by an additional 1 μL application of uranyl acetate. After 20 s, the excess uranyl acetate was blotted and permitted to air-dry until imaging. The TEM grids were imaged using a FEI Titan Halo 300 kV electron microscope at the Applied Science and Research Center (ASRC) at City University of New York (CUNY). These experiments were repeated using three grids per sample to confirm morphological characteristics.

Doxorubicin Binding and Release. To investigate the potential of F-TRAP as a drug delivery vehicle, TRAP and F-TRAP were incubated with free base Dox for assessment of loading efficiency and release. To determine the encapsulation efficiency of TRAP and F-TRAP, Dox was dissolved in DMSO and added to TRAP or F-TRAP at a 2:1 molar ratio of drug to protein (100 μM Dox:50 μM protein) in an amber tube and incubated at 4 °C for 12 h. Free Dox was removed *via* SEC using a G-25 medium Sephadex resin. The resin was hydrated in diH_2O overnight at room temperature before being added to a column (0.5 cm internal diameter, 15 cm length). The resin was equilibrated in degassed mobile phase buffer (50 mM Na_2HPO_4/0.5 M NaCl, pH 8.0) followed by application of the protein−drug complex. The mobile phase buffer was constantly added to maintain continuous flow and elution from the column. Elutions (1 mL each) were collected for absorbance readings of Dox at 485 nm.[111] Elution absorbances were compared to those of a standard curve of known Dox concentrations prepared in 50 mM Na_2HPO_4/0.5 M NaCl, pH 8.0, to determine Dox concentrations. Elution fractions with the highest absorbance values were also subjected to an enhanced BCA assay for assessment of protein concentration. The loading efficiency of Dox by TRAP and F-TRAP was calculated from the amount of Dox quantified in SEC elutions using the following equation:[112]

$$\text{Loading Efficiency (\%)} = 100 \times (\text{Amount of Dox Entrapped}/\text{Amount of Dox loaded})$$

The weighted loading was calculated as μg Dox per mg protein.[113]

Passive, room-temperature, release of Dox by TRAP and F-TRAP was assessed following passive loading of Dox at the corresponding loading efficiencies, determined by SEC studies, overnight. The protein−drug complex, or free base Dox alone as a control, was added to a 10 kDa MWCO dialysis membrane and suspended in 50 mM Na_2HPO_4/0.5 M NaCl, pH 8.0, at room temperature, with mixing at 80 rpm. Over a period of 24 h, samples were subjected to absorbance readings at 485 nm to measure the concentration of Dox remaining compared to a standard curve of known Dox concentrations also prepared in 50 mM Na_2HPO_4/0.5 M NaCl, pH 8.0. Released Dox was plotted as an accumulated percentage of the original amount of Dox loaded. The dialysis buffer outside of the membrane was replaced hourly for the first 8 h to spur drug release.

Dox release was further investigated under hyperthermic conditions in which TRAP or F-TRAP-bound Dox complexes were added to amber tubes in triplicate and suspended in a 45 °C water bath.[114] At 30 min, 1 h, and 2 h, one tube was removed from the water bath and centrifuged for 5 min at 13200 rpm to pellet the coacervate protein. The supernatant was subjected to absorbance readings at 485 nm.[114] The concentration of released Dox was compared to a standard curve of known Dox concentrations, and the amount of Dox released was plotted as an accumulated percentage of the original amount of Dox loaded.

Cell Viability Studies. MTT (3-(4,5-dimethylthiazol-2-yl)-2,5-diphenyltetrazolium bromide) cell viability assays were conducted to assess the efficacy of free and F-TRAP-delivered Dox on the MCF-7 breast adenocarcinoma cell line.[115] MCF-7 cells were seeded into a 96-well plate at a density of 10000 cells/well in minimum essential media (MEM) supplemented with 10% fetal bovine serum, 1% penicillin/streptomycin, and 0.01 mg mL^{-1} human recombinant insulin and incubated overnight at 37 °C with 5% CO_2. MEM was subsequently removed, and 90 μL of fresh MEM was added per well. Cells were treated with 10 μL of Dox, F-TRAP, or Dox-loaded F-TRAP (F-TRAP·Dox) in quadruplicates at increasing concentrations with a static final DMSO concentration of 0.55% v/v. Treated cells were incubated either for 48 h at 37 °C with 5% CO_2 or for 1 h in a 42 °C water bath followed by 37 °C with 5% CO_2 for 47 h. After treatment, the media was removed; the cells were rinsed once with 1× PBS, and 100 μL of fresh MEM was added per well. To assess the cytotoxicity of Dox and the Dox-loaded protein complexes, 10 μL of 5 mg/mL MTT stock in 1× PBS was added per well and incubated for 4 h at 37 °C with 5% CO_2. Following incubation, all but 25 μL of the medium was removed per well and 50 μL of DMSO was added per the manufacturer's protocol. Cells were incubated for 10 min at 37 °C with 5% CO_2. The absorbance of each well was assessed using a Biotek Synergy HT microplate reader at 540 nm. The cell viability of treated cells was calculated as a percentage normalized to untreated cell controls. Data represent the average of four replicates per sample per trial, and error bars represent the standard deviations.

Nuclear Magnetic Resonance Measurements. Limit of ^{19}F detection studies were conducted on a Bruker AVIII-400 (9.4 T) instrument equipped with a BB(F)O probehead. F-TRAP sensitivity was compared to the commercially available ^{19}F nanoemulsion V-Sense (Celsense) using a ^{19}F one-pulse sequence with the following parameters: echo time (TE) = 300 ms, flip angle (FA) = 90°, sweep width (SW) = 89.285 kHz, acquisition time = 0.73 s, with number of scans (NS) =264, resulting in an experiment time T_{IM} = 3 min 13 s. The 1D ^{19}F NMR spectra of F-TRAP and V-sense at ^{19}F concentrations ranging from 0.25 to 2.5 mM and 0.0025 to 1 mM, respectively, were acquired. A standard composed of 10% TFA/10% D_2O/80% H_2O, acquired with the same sequence, was used to calibrate all spectra in Topspin 3.2 software. Topspin 3.2 was further used to quantify SNRs, calculated *via* the Bruker SINO command to identify the LOD, the concentration at which the SNR is equal to 3.[88−91] The Bruker PEAKW command was employed to determine the fwhm for F-TRAP and V-Sense. The intensities of the F-TRAP peaks were quantified using Bruker's integration function. 1D ^{19}F NMR spectra of F-TRAP samples at 1 mg/mL protein concentration were also obtained as a function of temperature at 26.85 °C (300 K), 31.85 °C (305 K), and 37.0 °C (310.15 K), each calibrated to a 10% trifluoroethanol/10% D_2O/80% H_2O standard acquired at the corresponding temperature using the identical sequence. Both the F-TRAP sample and calibration standard were acquired using the above-described ^{19}F one-pulse sequence. Topspin 3.2 software was used to overlay the spectra acquired at variable temperatures.

The relaxation properties of F-TRAP were obtained as a function of temperature on a 500 MHz (11.7 T) Bruker Avance II instrument equipped with a 5 mm room-temperature BB(F)O SMART probe. Both the inversion recovery and CPMG ^{19}F NMR experiments[58] were performed on F-TRAP at 0.5, 0.6, 0.75, and 0.9 mg/mL (corresponding to 0.82 mM ^{19}F, 0.98 mM ^{19}F, 1.23 mM ^{19}F, and 1.47 mM ^{19}F) at varying temperatures (21.85, 26.85, 31.85, 37 °C). Inversion recovery experiments were used to determine the T_1 relaxation times with an SW of 38 311 Hz (corresponding to 76.6219 ppm) and delay time of 2.0 s with 1024 scans at each of the following variable delay times: 0.001, 0.05, 0.1, 0.2, 0.3, 0.5, 0.8, 1.0, 1.5, 2.0, 2.5, 3.0, 3.5, 4.0, 4.5, 5.0 s. CPMG experiments were used to determine the T_2 relaxation times with an SW of 38 311 Hz (corresponding to 76.6219 ppm) and delay time of 2.0 and 1024 scans at each of the following variable counter times: 2, 20, 50, 100, 200, 400, 600, 800, 1000, 1400, 1600, 1800, 2500 μs. The relaxation times (T_1 and T_2) were calculated by using curve fitting analysis in Topspin 3.2 software.

Phantom Magnetic Resonance Experiments. Magnetic resonance imaging was conducted using ^1H nuclei to identify all samples containing water and using ^{19}F nuclei to locate and quantify the sample containing ^{19}F-TRAP. All MRI experiments were performed on a Biospec 7030 micro-MRI system (Bruker) composed of an Avance-3 HD console and a zero-boil-off 7 T (300 MHz) 300 mm horizontal bore magnet equipped with an actively shielded gradient coil insert (Bruker BGA-12S-HP; i.d. 114 mm, 660 mT/m gradient strength, 130 μs rise time). The MRI experiments were performed with a house-made whole body birdcage coil inductively coupled to a slotted resonator, capable of holding two glass tubes (o.d. 6 mm) and broadband tuning *via* a variable capacitor to cover both Larmor frequencies of ^1H proton (300.16 MHz) and ^{19}F (282.4

DOI: 10.1021/acsnano.8b07481
ACS Nano 2019, 13, 2969−2985

MHz) at 7 T (Figure 6C). The coil was first tuned and matched for ^{1}H for rapid scout scans due to the greater proton signal sensitivity, which was used as a spatial reference for ^{19}F scans.

ZTE imaging was employed for ^{1}H and ^{19}F imaging (repetition time (TR) = 2.5 ms, TE = 20 μs, FA = 4°, SW = 100 kHz, NS = 128, resulting in 781 Hz/pixel) with the number of repetitions (NR) = 1 and T_{IM} = 32 s for ^{1}H imaging and NR = 110 and T_{IM} = 1 h for ^{19}F imaging. The ZTE imaging sequence is based on a 3D radial acquisition method for which center-out readouts are performed in the presence of a constant gradient in a steady state of the magnetization. A nonselective excitation with very short RF pulse was employed in order to capture signals with extremely short T_2 values (TE = 20 μs), while a very small flip angle (FA = 4°) in combination with a very short repetition time (TR = 2.5 ms) was used to achieve efficient SNR scanning. Despite the apparent high duty cycle, the very short RF excitation pulse, in combination with the low flip angle used, prevented any RF-induced heating effect as assessed by the continuous monitoring of the temperature of the sample imaged.

For imaging experiments, a set of solutions with concentrations ranging from 5 to 13.40 mg/mL F-TRAP (equivalent to 8.17 mM ^{19}F and 21.90 mM ^{19}F, respectively), at a total volume of ∼500 μL, and a negative control volume of water were placed in separate 5 mm NMR tubes. The temperature of the 5 mm glass tubes containing the F-TRAP solutions was systematically and continuously monitored during the MRI scans *via* a thermocouple probe implanted at the tip of the NMR glass tube across the rubber cap to ensure proper sealing. No temperature changes that may be induced by RF heating were observed during the MRI scans.

The 13.40 mg/mL F-TRAP phantom sample was also acquired using a ^{19}F MRS sequence on the same 7 T (300 MHz) system (TR = 2000 ms, NS = 200, FA = 90°, T_{IM} = 6 min 40 s). The MRS spectra was calibrated in Topspin 3.2 software to a standard composed of 10% TFA/90% H_2O acquired with the same sequence.

Endotoxin Removal. Pierce high-capacity endotoxin removal spin columns were used to remove endotoxins from the F-TRAP sample to be studied *in vivo*. After regeneration with 0.2 N NaOH, endotoxin removal resin was washed using 2 M NaCl solution, followed by endotoxin-free, ultrapure water. The resin was then equilibrated with endotoxin-free 1× PBS, pH 7.4, for a total of three times. The protein sample at a concentration of 2.7 mg/mL was added to the resin and incubated for 1 h at 4 °C. The sample was eluted in a sterile 15 mL tube *via* centrifugation at 500*g* for 1 min.

Near-Infrared Fluorochrome Conjugation. Endotoxin-free F-TRAP was subsequently diluted in endotoxin-free 50 mM carbonate/bicarbonate buffer, pH 8.5, to 1 mg/mL and conjugated to the NIR fluorochrome VivoTag-S 750 (PerkinElmer) at room temperature for 1 h using end-over-end mixing (Labquake Rotisserie, Barnstead Thermolyne). Nonconjugated fluorochrome was removed using an Amicon Ultra-15 centrifugal filter 3 kDa MWCO, while buffer exchanging fluorochrome-conjugated F-TRAP (NIR-F-TRAP) into endotoxin-free 1× PBS, pH 7.4, and concentrating to 13.40 mg/mL.

***In Vivo* Experiments.** The use of F-TRAP for *in vivo* tumor imaging was assessed in an MCF-7 xenograft mouse model using optical imaging and magnetic resonance imaging. Animal work was performed in strict accordance with the National Institutes of Health Guide for the Care and Use of Laboratory Animals and using procedures approved by the Institutional Animal Care and Use Committee at the New York University School of Medicine. At 4−6 weeks old, female CrTac:NCr-*Foxn1*^{nu} nude mice acquired from Taconic Biosciences were injected with 3 × 10^6 MCF-7 cells embedded in 150 μL Corning Matrigel matrix. One week after MCF-7 cell injection, mice were injected over the right scapula with Matrigel embedded with 100 μg of β-estradiol twice a week. Tumors were permitted to grow until a 5 mm diameter, or 100 mm^3 volume, was reached as measured *via* high-frequency ultrasound (Fujifilm Vevo 3100 VisualSonic Ultrasound) prior to ultrasound-guided intratumoral injection of endotoxin-free NIR-F-TRAP. Mice were anesthetized with a cocktail of ketamine (100 mg/mL)/xylazine (20 mg/mL) at 0.1 mL/g mouse weight. Prior to injecting NIR-F-TRAP, mice were subjected to baseline *in vivo* multispectral vis−NIR fluorescence imaging overlaid onto an anatomical reflectance image on a Bruker In-Vivo Xtreme, with an excitation of 730 nm and emission acquisition at 790 nm over 30 s exposure. Mice were subsequently injected with 50 μL of 13.40 mg/mL NIR-F-TRAP (equivalent to 0.82 mM F-TRAP and 21.90 mM ^{19}F) intratumorally under high-frequency ultrasound using a microfine 26 gauge 1/2 in. needle and immediately reimaged using dual fluorescence−reflectance imaging. A 24 h post-injection fluorescence−reflectance image was also acquired to confirm clearance of the construct. All fluorescence images were presented on the same intensity scale provided in picowatts per mm^2.

In vivo ^{1}H MR imaging and ^{19}F MRS of NIR-F-TRAP were conducted immediately following fluorescence−reflectance imaging using a house-made setup composed of a ^{19}F-tunable house-made low-pass ladder surface coil inductively coupled to the same homemade birdcage coil used for phantom imaging, which was placed directly over the tumor. The tumor was visualized using a standard ^{1}H T_1-weighted 3D FLASH imaging sequence (TR = 610.94 ms, TE = 2 ms, FA = 30°, matrix = (256 mm)^3, resolution = (234.375 μm)^3, SW = 67 kHz, T_{IM} = 1 min, 18 s), and NIR-F-TRAP injected into the tumor was detected using a ^{19}F MRS sequence (TR = 2000 ms, NS = 200, FA = 90°, T_{IM} = 6 min 40 s), which maintained a higher sensitivity than was obtainable with ^{19}F MR imaging. The MRS spectra were calibrated in Topspin 3.2 software to a standard composed of 10% TFA/90% H_2O acquired with the same sequence.

ASSOCIATED CONTENT

Supporting Information

The Supporting Information is available free of charge on the ACS Publications website at DOI: 10.1021/acsnano.8b07481.

Supporting figures and tables related to MALDI-TOF MS, protein expression yields, protein purification, turbidity, CD deconvolution, TEM, DLS, NMR, MRS, MRI, ultrasound, vis−NIR fluorescence and reflectance imaging, and doxorubicin loading efficiency (PDF)

AUTHOR INFORMATION

Corresponding Authors

*E-mail: Youssef.ZaimWadghiri@nyulangone.org.
*E-mail: Montclare@nyu.edu.

ORCID

Jin Kim Montclare: 0000-0001-6857-3591

Author Contributions

○L. K. Hill and J. A. Frezzo contributed equally to this work.

Notes

The authors declare no competing financial interest.

ACKNOWLEDGMENTS

This work was supported by the NSF-MRSEC Program under Award Number DMR 1420073, NSF-DMREF under Award Number DMR 1728858, the NYU Shiffrin-Myers Breast Cancer Discovery Fund, and the NYU CTSA grant UL1 TR000038 from the National Center for Advancing Translational Sciences, National Institutes of Health. Some of the experiments were performed at the NYU Langone Health Preclinical Imaging Laboratory, a shared resource partially supported by the NIH/SIG 1S10OD018337-01, the Laura and Isaac Perlmutter Cancer Center Support Grant NIH/NCI 5P30CA016087, and the NIBIB Biomedical Technology Resource Center Grant NIH P41 EB017183. The authors thank J. Schulze at the Molecular Structure Facility at UC Davis for assistance in AAA, C. Lin for his guidance with ^{19}F NMR and subsequent analysis, J. Baquero Buitrago for

DOI: 10.1021/acsnano.8b07481
ACS Nano 2019, 13, 2969−2985

supplying us with the MCF-7 xenograft CrTac:NCr-*Foxn1*^{nu} mice, and O. Aristizábal for his assistance with ultrasound-guided intratumoral injection and training on the Bruker *In Vivo* Xtreme II.

REFERENCES

(1) Deans, A. E.; Wadghiri, Y. Z.; Bernas, L. M.; Yu, X.; Rutt, B. K.; Turnbull, D. H. Cellular MRI Contrast *via* Coexpression of Transferrin Receptor and Ferritin. *Magn. Reson. Med.* **2006**, *56*, 51−59.

(2) Korkusuz, H.; Ulbrich, K.; Welzel, K.; Koeberle, V.; Watcharin, W.; Bahr, U.; Chernikov, V.; Knobloch, T.; Petersen, S.; Huebner, F.; Ackermann, H.; Gelperina, S.; Kromen, W.; Hammerstingl, R.; Haupenthal, J.; Gruenwald, F.; Fiehler, J.; Zeuzem, S.; Kreuter, J.; Vogl, T. J.; Piiper, A. Transferrin-Coated Gadolinium Nanoparticles as MRI Contrast Agent. *Mol. Imaging Biol.* **2013**, *15*, 148−154.

(3) Kremer, S.; Lamy, J.; Magnus, A.; Oesterle, H.; Jeantroux, J.; Trunet, S.; Armspach, J.-P.; Dietemann, J.-L.; de Sèze, J. Evaluation of an Albumin-Binding Gadolinium Contrast Agent in Multiple Sclerosis. *Neurology* **2013**, *81*, 206−210.

(4) Montclare, J. K.; Tirrell, D. A. Evolving Proteins of Novel Composition. *Angew. Chem., Int. Ed.* **2006**, *45*, 4518−4521.

(5) Haghpanah, J. S.; Yuvienco, C.; Civay, D. E.; Barra, H.; Baker, P. J.; Khapli, S.; Voloshchuk, N.; Gunasekar, S. K.; Muthukumar, M.; Montclare, J. K. Artificial Protein Block Copolymers Blocks Comprising Two Distinct Self-Assembling Domains. *ChemBioChem* **2009**, *10*, 2733−2735.

(6) Dai, M.; Haghpanah, J.; Singh, N.; Roth, E. W.; Liang, A.; Tu, R. S.; Montclare, J. K. Artificial Protein Block Polymer Libraries Bearing Two SADs: Effects of Elastin Domain Repeats. *Biomacromolecules* **2011**, *12*, 4240−4246.

(7) Yuvienco, C.; More, H. T.; Haghpanah, J. S.; Tu, R. S.; Montclare, J. K. Modulating Supramolecular Assemblies and Mechanical Properties of Engineered Protein Materials by Fluorinated Amino Acids. *Biomacromolecules* **2012**, *13*, 2273−2278.

(8) Montclare, J. K.; Son, S.; Clark, G. A.; Kumar, K.; Tirrell, D. A. Biosynthesis and Stability of Coiled-Coil Peptides Containing (2S,4R)-5,5,5-Trifluoroleucine and (2S,4S)-5,5,5-Trifluoroleucine. *ChemBioChem* **2009**, *10*, 84−86.

(9) More, H. T.; Zhang, K. S.; Srivastava, N.; Frezzo, J. A.; Montclare, J. K. Influence of Fluorination on Protein-Engineered Coiled-Coil Fibers. *Biomacromolecules* **2015**, *16*, 1210−1217.

(10) Panchenko, T.; Zhu, W. W.; Montclare, J. K. Influence of Global Fluorination on Chloramphenicol Acetyltransferase Activity and Stability. *Biotechnol. Bioeng.* **2006**, *94*, 921−930.

(11) Voloshchuk, N.; Montclare, J. K. Incorporation of Unnatural Amino Acids for Synthetic Biology. *Mol. BioSyst.* **2010**, *6*, 65−80.

(12) Voloshchuk, N.; Lee, M. X.; Zhu, W. W.; Tanrikulu, I. C.; Montclare, J. K. Fluorinated Chloramphenicol Acetyltransferase Thermostability and Activity Profile: Improved Thermostability by a Single-Isoleucine Mutant. *Bioorg. Med. Chem. Lett.* **2007**, *17*, 5907−5911.

(13) Yin, L.; Yuvienco, C.; Montclare, J. K. Protein Based Therapeutic Delivery Agents: Contemporary Developments and Challenges. *Biomaterials* **2017**, *134*, 91−116.

(14) van Zijl, P. C. M.; Yadav, N. N. Chemical Exchange Saturation Transfer (CEST): What Is in a Name and What Isn't? *Magn. Reson. Med.* **2011**, *65*, 927−948.

(15) Schmiedl, U.; Ogan, M.; Paajanen, H.; Marotti, M.; Crooks, L. E.; Brito, A. C.; Brasch, R. C. Albumin Labeled with Gd-DTPA as an Intravascular, Blood Pool-Enhancing Agent for MR Imaging: Biodistribution and Imaging Studies. *Radiology* **1987**, *162*, 205−210.

(16) Bogdanov, A. A.; Weissleder, R.; Frank, H. W.; Bogdanova, A. V.; Nossif, N.; Schaffer, B. K.; Tsai, E.; Papisov, M. I.; Brady, T. J. A New Macromolecule as a Contrast Agent for MR Angiography: Preparation, Properties, and Animal Studies. *Radiology* **1993**, *187*, 701−706.

(17) Wadghiri, Y. Z.; Sigurdsson, E. M.; Sadowski, M.; Elliott, J. I.; Li, Y.; Scholtzova, H.; Tang, C. Y.; Aguinaldo, G.; Pappolla, M.; Duff, K.; Wisniewski, T.; Turnbull, D. H. Detection of Alzheimer's Amyloid in Transgenic Mice Using Magnetic Resonance Microimaging. *Magn. Reson. Med.* **2003**, *50*, 293−302.

(18) Artemov, D.; Mori, N.; Ravi, R.; Bhujwalla, Z. M. Magnetic Resonance Molecular Imaging of the HER-2/Neu Receptor. *Cancer Res.* **2003**, *63*, 2723−2727.

(19) Mulder, W. J. M.; Strijkers, G. J.; Habets, J. W.; Bleeker, E. J. W.; van der Schaft, D. W. J.; Storm, G.; Koning, G. A.; Griffioen, A. W.; Nicolay, K. MR Molecular Imaging and Fluorescence Microscopy for Identification of Activated Tumor Endothelium Using a Bimodal Lipidic Nanoparticle. *FASEB J.* **2005**, *19*, 2008−2010.

(20) Wadghiri, Y. Z.; Li, J.; Wang, J.; Hoang, D. M.; Sun, Y.; Xu, H.; Tsui, W.; Li, Y.; Boutajangout, A.; Wang, A.; de Leon, M.; Wisniewski, T. Detection of Amyloid Plaques Targeted by Bifunctional USPIO in Alzheimer's Disease Transgenic Mice Using Magnetic Resonance Microimaging. *PLoS One* **2013**, *8*, No. e57097.

(21) Marsh, E. N. G.; Suzuki, Y. Using (19)F NMR to Probe Biological Interactions of Proteins and Peptides. *ACS Chem. Biol.* **2014**, *9*, 1242−1250.

(22) Yu, J.-X.; Hallac, R. R.; Chiguru, S.; Mason, R. P. New Frontiers and Developing Applications in 19F NMR. *Prog. Nucl. Magn. Reson. Spectrosc.* **2013**, *70*, 25−49.

(23) Srinivas, M.; Boehm-Sturm, P.; Figdor, C. G.; de Vries, I. J.; Hoehn, M. Labeling Cells for *In Vivo* Tracking Using (19)F MRI. *Biomaterials* **2012**, *33*, 8830−8840.

(24) Ahrens, E. T.; Bulte, J. W. M. Tracking Immune Cells *In Vivo* Using Magnetic Resonance Imaging. *Nat. Rev. Immunol.* **2013**, *13*, 755−763.

(25) Ratner, A. V.; Quay, S.; Muller, H. H.; Simpson, B. B. 19F Relaxation Rate Enhancement and Frequency Shift with Gd-DTPA. *Invest. Radiol.* **1989**, *24*, 224−227.

(26) *Fluorine Magnetic Resonance Imaging*; Flögel, U.; Ahrens, E., Eds.; Pan Stanford: New York, 2016.

(27) Flögel, U.; Ding, Z.; Hardung, H.; Jander, S.; Reichmann, G.; Jacoby, C.; Schubert, R.; Schrader, J. *In Vivo* Monitoring of Inflammation after Cardiac and Cerebral Ischemia by Fluorine Magnetic Resonance Imaging. *Circulation* **2008**, *118*, 140−148.

(28) Janjic, J. M.; Srinivas, M.; Kadayakkara, D. K. K.; Ahrens, E. T. Self-Delivering Nanoemulsions for Dual Fluorine-19 MRI and Fluorescence Detection. *J. Am. Chem. Soc.* **2008**, *130*, 2832−2841.

(29) Ruiz-Cabello, J.; Walczak, P.; Kedziorek, D. A.; Chacko, V. P.; Schmieder, A. H.; Wickline, S. A.; Lanza, G. M.; Bulte, J. W. M. *In Vivo* "Hot Spot" MR Imaging of Neural Stem Cells Using Fluorinated Nanoparticles. *Magn. Reson. Med.* **2008**, *60*, 1506−1511.

(30) Moonshi, S. S.; Zhang, C.; Peng, H.; Puttick, S.; Rose, S.; Fisk, N. M.; Bhakoo, K.; Stringer, B. W.; Qiao, G. G.; Gurr, P. A.; Whittaker, A. K. A Unique 19F MRI Agent for the Tracking of Non Phagocytic Cells *In Vivo*. *Nanoscale* **2018**, *10*, 8226−8239.

(31) Yu, M.; Bouley, B. S.; Xie, D.; Enriquez, J. S.; Que, E. L. 19F PARASHIFT Probes for Magnetic Resonance Detection of H2O2 and Peroxidase Activity. *J. Am. Chem. Soc.* **2018**, *140*, 10546−10552.

(32) Guo, C.; Xu, S.; Arshad, A.; Wang, L. A PH-Responsive Nanoprobe for Turn-on 19F-Magnetic Resonance Imaging. *Chem. Commun.* **2018**, *54*, 9853−9856.

(33) Zhang, C.; Moonshi, S. S.; Wang, W.; Ta, H. T.; Han, Y.; Han, F. Y.; Peng, H.; Král, P.; Rolfe, B. E.; Gooding, J. J.; Gaus, K.; Whittaker, A. K. High F-Content Perfluoropolyether-Based Nanoparticles for Targeted Detection of Breast Cancer by 19F Magnetic Resonance and Optical Imaging. *ACS Nano* **2018**, *12*, 9162−9176.

(34) Iima, R.; Takegami, S.; Konishi, A.; Tajima, S.; Minematsu, N.; Kitade, T. Thermal Behavior of 19F Nuclear Magnetic Resonance Signal of 19F-Containing Compound in Lipid Nano-Emulsion for Potential Tumor Diagnosis. *AAPS PharmSciTech* **2018**, *19*, 2679−2686.

(35) Huang, P.; Guo, W.; Yang, G.; Song, H.; Wang, Y.; Wang, C.; Kong, D.; Wang, W. Fluorine Meets Amine: Reducing Microenvironment-Induced Amino-Activatable Nanoprobes for 19F-Magnetic

DOI: 10.1021/acsnano.8b07481
ACS Nano 2019, 13, 2969−2985

Resonance Imaging of Biothiols. *ACS Appl. Mater. Interfaces* **2018**, *10*, 18532−18542.
(36) Shin, S. H.; Park, E.-J.; Min, C.; Choi, S. I.; Jeon, S.; Kim, Y.-H.; Kim, D. Tracking Perfluorocarbon Nanoemulsion Delivery by 19F MRI for Precise High Intensity Focused Ultrasound Tumor Ablation. *Theranostics* **2017**, *7*, 562−572.
(37) Ko, I. O.; Jung, K.-H.; Kim, M. H.; Kang, K. J.; Lee, K. C.; Kim, K. M.; Noh, I.; Lee, Y. J.; Lim, S. M.; Kim, J. Y.; Park, J.-A. Preliminary 19F-MRS Study of Tumor Cell Proliferation with 3′-Deoxy-3′-Fluorothymidine and Its Metabolite (FLT-MP). *Contrast Media Mol. Imaging* **2017**, *2017*, 1−7.
(38) Makela, A. V.; Foster, P. J. Imaging Macrophage Distribution and Density in Mammary Tumors and Lung Metastases Using Fluorine-19 MRI Cell Tracking. *Magn. Reson. Med.* **2018**, *80*, 1138−1147.
(39) Constantinides, C.; Basnett, P.; Lukasiewicz, B.; Carnicer, R.; Swider, E.; Majid, Q. A.; Srinivas, M.; Carr, C. A.; Roy, I. *In Vivo* Tracking and 1H/19F Magnetic Resonance Imaging of Biodegradable Polyhydroxyalkanoate/Polycaprolactone Blend Scaffolds Seeded with Labeled Cardiac Stem Cells. *ACS Appl. Mater. Interfaces* **2018**, *10*, 25056−25068.
(40) Shi, Y.; Oeh, J.; Hitz, A.; Hedehus, M.; Eastham-Anderson, J.; Peale, F. V.; Hamilton, P.; O'Brien, T.; Sampath, D.; Carano, R. A. D. Monitoring and Targeting Anti-VEGF Induced Hypoxia within the Viable Tumor by 19F-MRI and Multispectral Analysis. *Neoplasia* **2017**, *19*, 950−959.
(41) Temme, S.; Grapentin, C.; Quast, C.; Jacoby, C.; Grandoch, M.; Ding, Z.; Owenier, C.; Mayenfels, F.; Fischer, J. W.; Schubert, R.; Schrader, J.; Flögel, U. Noninvasive Imaging of Early Venous Thrombosis by 19F Magnetic Resonance Imaging with Targeted Perfluorocarbon Nanoemulsions. *Circulation* **2015**, *131*, 1405−1414.
(42) Zhang, F.; Zhou, Q.; Yang, G.; An, L.; Li, F.; Wang, J. A Genetically Encoded 19F NMR Probe for Lysine Acetylation. *Chem. Commun.* **2018**, *54*, 3879−3882.
(43) Hu, J.; Wu, Q.; Cheng, K.; Xie, Y.; Li, C.; Li, Z. A^{19} F NMR Probe for the Detection of β-Galactosidase: Simple Structure with Low Molecular Weight of 274.2, "Turn-on" Signal without the Background, and Good Performance Applicable in Cancer Cell Line. *J. Mater. Chem. B* **2017**, *5*, 4673−4678.
(44) Yuan, Y.; Ge, S.; Sun, H.; Dong, X.; Zhao, H.; An, L.; Zhang, J.; Wang, J.; Hu, B.; Liang, G. Intracellular Self-Assembly and Disassembly of (19)F Nanoparticles Confer Respective "Off" and "On" (19)F NMR/MRI Signals for Legumain Activity Detection in Zebrafish. *ACS Nano* **2015**, *9*, 5117−5124.
(45) Wang, H.; Raghupathi, K. R.; Zhuang, J.; Thayumanavan, S. Activatable Dendritic (19)F Probes for Enzyme Detection. *ACS Macro Lett.* **2015**, *4*, 422−425.
(46) Vernikouskaya, I.; Pochert, A.; Lindén, M.; Rasche, V. Quantitative 19F MRI of Perfluoro-15-Crown-5-Ether Using Uniformity Correction of the Spin Excitation and Signal Reception. *MAGMA* **2018**, *1−12*, DOI: 10.1007/s10334-018-0696-6.
(47) Xu, M.; Guo, C.; Hu, G.; Xu, S.; Wang, L. Organic Nanoprobes for Fluorescence and^{19} F Magnetic Resonance Dual-Modality Imaging. *Chin. J. Chem.* **2018**, *36*, 25−30.
(48) Bo, S.; Yuan, Y.; Chen, Y.; Yang, Z.; Chen, S.; Zhou, X.; Jiang, Z.-X. *In Vivo* Drug Tracking with 19F MRI at Therapeutic Dose. *Chem. Commun.* **2018**, *54*, 3875−3878.
(49) Kolouchova, K.; Sedlacek, O.; Jirak, D.; Babuka, D.; Blahut, J.; Kotek, J.; Vit, M.; Trousil, J.; Konefał, R.; Janouskova, O.; Podhorska, B.; Slouf, M.; Hruby, M. Self-Assembled Thermoresponsive Polymeric Nanogels for 19F MR Imaging. *Biomacromolecules* **2018**, *19*, 3515−3524.
(50) Ashur, I.; Allouche-Arnon, H.; Bar-Shir, A. Calcium Fluoride Nanocrystals: Tracers for *In Vivo* ^{19} F Magnetic Resonance Imaging. *Angew. Chem.* **2018**, *130*, 7600−7604.
(51) Kirberger, S. E.; Maltseva, S. D.; Manulik, J. C.; Einstein, S. A.; Weegman, B. P.; Garwood, M.; Pomerantz, W. C. K. Synthesis of Intrinsically Disordered Fluorinated Peptides for Modular Design of High-Signal 19 F MRI Agents. *Angew. Chem., Int. Ed.* **2017**, *56*, 6440−6444.
(52) Jackson, J. C.; Hammill, J. T.; Mehl, R. A. Site-Specific Incorporation of a (19)F-Amino Acid into Proteins as an NMR Probe for Characterizing Protein Structure and Reactivity. *J. Am. Chem. Soc.* **2007**, *129*, 1160−1166.
(53) Gee, C. T.; Arntson, K. E.; Urick, A. K.; Mishra, N. K.; Hawk, L. M. L.; Wisniewski, A. J.; Pomerantz, W. C. K. Protein-Observed (19)F-NMR for Fragment Screening, Affinity Quantification and Druggability Assessment. *Nat. Protoc.* **2016**, *11*, 1414−1427.
(54) Preslar, A. T.; Tantakitti, F.; Park, K.; Zhang, S.; Stupp, S. I.; Meade, T. J. (19)F Magnetic Resonance Imaging Signals from Peptide Amphiphile Nanostructures Are Strongly Affected by Their Shape. *ACS Nano* **2016**, *10*, 7376−7384.
(55) Hawk, L. M. L.; Gee, C. T.; Urick, A. K.; Hu, H.; Pomerantz, W. C. K. Paramagnetic Relaxation Enhancement for Protein-Observed 19F NMR as an Enabling Approach for Efficient Fragment Screening. *RSC Adv.* **2016**, *6*, 95715−95721.
(56) Hansen, P. R.; Oddo, A. Fmoc Solid-Phase Peptide Synthesis. *Methods Mol. Biol.* **2015**, *1348*, 33−50.
(57) Tang, Y.; Tirrell, D. A. Biosynthesis of a Highly Stable Coiled-Coil Protein Containing Hexafluoroleucine in an Engineered Bacterial Host. *J. Am. Chem. Soc.* **2001**, *123*, 11089−11090.
(58) Aramini, J. M.; Hamilton, K.; Ma, L.-C.; Swapna, G. V. T.; Leonard, P. G.; Ladbury, J. E.; Krug, R. M.; Montelione, G. T. (19)F NMR Reveals Multiple Conformations at the Dimer Interface of the Nonstructural Protein 1 Effector Domain from Influenza A Virus. *Structure* **2014**, *22*, 515−525.
(59) Chalmers, K. H.; De Luca, E.; Hogg, N. H. M.; Kenwright, A. M.; Kuprov, I.; Parker, D.; Botta, M.; Wilson, J. I.; Blamire, A. M. Design Principles and Theory of Paramagnetic Fluorine-Labelled Lanthanide Complexes as Probes for (19)F Magnetic Resonance: A Proof-of-Concept Study. *Chem. - Eur. J.* **2010**, *16*, 134−148.
(60) Srivastava, K.; Weitz, E. A.; Peterson, K. L.; Marjańska, M.; Pierre, V. C. Fe- and Ln-DOTAm-F12 Are Effective Paramagnetic Fluorine Contrast Agents for MRI in Water and Blood. *Inorg. Chem.* **2017**, *56*, 1546−1557.
(61) Kelkar, S. S.; Reineke, T. M. Theranostics: Combining Imaging and Therapy. *Bioconjugate Chem.* **2011**, *22*, 1879−1903.
(62) Gunasekar, S. K.; Anjia, L.; Matsui, H.; Montclare, J. K. Effects of Divalent Metals on Nanoscopic Fiber Formation and Small Molecule Recognition of Helical Proteins. *Adv. Funct. Mater.* **2012**, *22*, 2154−2159.
(63) Gunasekar, S. K.; Asnani, M.; Limbad, C.; Haghpanah, J. S.; Hom, W.; Barra, H.; Nanda, S.; Lu, M.; Montclare, J. K. N-Terminal Aliphatic Residues Dictate the Structure, Stability, Assembly, and Small Molecule Binding of the Coiled-Coil Region of Cartilage Oligomeric Matrix Protein. *Biochemistry* **2009**, *48*, 8559−8567.
(64) Haghpanah, J. S.; Yuvienco, C.; Roth, E. W.; Liang, A.; Tu, R. S.; Montclare, J. K. Supramolecular Assembly and Small Molecule Recognition by Genetically Engineered Protein Block Polymers Composed of Two SADs. *Mol. BioSyst.* **2010**, *6*, 1662−1667.
(65) Yin, L.; Agustinus, A. S.; Yuvienco, C.; Minashima, T.; Schnabel, N. L.; Kirsch, T.; Montclare, J. K. Engineered Coiled-Coil Protein for Delivery of Inverse Agonist for Osteoarthritis. *Biomacromolecules* **2018**, *19*, 1614−1624.
(66) Liu, C. F.; Chen, R.; Frezzo, J. A.; Katyal, P.; Hill, L. K.; Yin, L.; Srivastava, N.; More, H. T.; Renfrew, P. D.; Bonneau, R.; Montclare, J. K. Efficient Dual SiRNA and Drug Delivery Using Engineered Lipoproteoplexes. *Biomacromolecules* **2017**, *18*, 2688−2698.
(67) Speth, P. A.; van Hoesel, Q. G.; Haanen, C. Clinical Pharmacokinetics of Doxorubicin. *Clin. Pharmacokinet.* **1988**, *15*, 15−31.
(68) Tsai, C. J.; Li, J.; Gonzalez-Angulo, A. M.; Allen, P. K.; Woodward, W. A.; Ueno, N. T.; Lucci, A.; Krishnamurthy, S.; Gong, Y.; Yang, W.; Cristofanilli, M.; Valero, V.; Buchholz, T. A. Outcomes After Multidisciplinary Treatment of Inflammatory Breast Cancer in the Era of Neoadjuvant HER2-Directed Therapy. *Am. J. Clin. Oncol.* **2015**, *38*, 242−247.

DOI: 10.1021/acsnano.8b07481
ACS Nano 2019, 13, 2969−2985

(69) Kim, M. K.; Kang, Y. K. Positional Preference of Proline in Alpha-Helices. *Protein Sci.* **1999**, *8*, 1492−1499.
(70) Gaucher, G.; Dufresne, M.-H.; Sant, V. P.; Kang, N.; Maysinger, D.; Leroux, J.-C. Block Copolymer Micelles: Preparation, Characterization and Application in Drug Delivery. *J. Controlled Release* **2005**, *109*, 169−188.
(71) Fang, J.; Sawa, T.; Maeda, H. Factors and Mechanism of "EPR" Effect and the Enhanced Antitumor Effects of Macromolecular Drugs Including SMANCS. *Polymer Drugs in the Clinical Stage* **2004**, *519*, 29−49.
(72) Mohan, P.; Rapoport, N. Doxorubicin as a Molecular Nanotheranostic Agent: Effect of Doxorubicin Encapsulation in Micelles or Nanoemulsions on the Ultrasound-Mediated Intracellular Delivery and Nuclear Trafficking. *Mol. Pharmaceutics* **2010**, *7*, 1959−1973.
(73) Bandyopadhyay, A.; Wang, L.; Agyin, J.; Tang, Y.; Lin, S.; Yeh, I.-T.; De, K.; Sun, L.-Z. Doxorubicin in Combination with a Small TGFbeta Inhibitor: A Potential Novel Therapy for Metastatic Breast Cancer in Mouse Models. *PLoS One* **2010**, *5*, No. e10365.
(74) Trabbic-Carlson, K.; Meyer, D. E.; Liu, L.; Piervincenzi, R.; Nath, N.; LaBean, T.; Chilkoti, A. Effect of Protein Fusion on the Transition Temperature of an Environmentally Responsive Elastin-like Polypeptide: A Role for Surface Hydrophobicity? *Protein Eng., Des. Sel.* **2004**, *17*, 57−66.
(75) Garanger, E.; MacEwan, S. R.; Sandre, O.; Brûlet, A.; Bataille, L.; Chilkoti, A.; Lecommandoux, S. Structural Evolution of a Stimulus-Responsive Diblock Polypeptide Micelle by Temperature Tunable Compaction of Its Core. *Macromolecules* **2015**, *48*, 6617−6627.
(76) Meyer, D. E.; Chilkoti, A. Quantification of the Effects of Chain Length and Concentration on the Thermal Behavior of Elastin-like Polypeptides. *Biomacromolecules* **2004**, *5*, 846−851.
(77) Louis-Jeune, C.; Andrade-Navarro, M. A.; Perez-Iratxeta, C. Prediction of Protein Secondary Structure from Circular Dichroism Using Theoretically Derived Spectra. *Proteins: Struct., Funct., Genet.* **2012**, *80*, 374−381.
(78) Thorsteinsson, M. V.; Richter, J.; Lee, A. L.; DePhillips, P. 5-Dodecanoylaminofluorescein as a Probe for the Determination of Critical Micelle Concentration of Detergents Using Fluorescence Anisotropy. *Anal. Biochem.* **2005**, *340*, 220−225.
(79) Olsen, A. J.; Katyal, P.; Haghpanah, J. S.; Kubilius, M. B.; Li, R.; Schnabel, N. L.; O'Neill, S. C.; Wang, Y.; Dai, M.; Singh, N.; Tu, R. S.; Montclare, J. K. Protein Engineered Triblock Polymers Composed of Two Sads: Enhanced Mechanical Properties and Binding Abilities. *Biomacromolecules* **2018**, *19*, 1552−1561.
(80) Mukerjee, P. Fluorocarbon—hydrocarbon Interactions in Micelles and Other Lipid Assemblies, at Interfaces, and in Solutions. *Colloids Surf., A* **1994**, *84*, 1−10.
(81) Kim, W.; Thévenot, J.; Ibarboure, E.; Lecommandoux, S.; Chaikof, E. L. Self-Assembly of Thermally Responsive Amphiphilic Diblock Copolypeptides into Spherical Micellar Nanoparticles. *Angew. Chem., Int. Ed.* **2010**, *49*, 4257−4260.
(82) Gillies, E. R.; Fréchet, J. M. J. A New Approach towards Acid Sensitive Copolymer Micelles for Drug Delivery. *Chem. Commun.* **2003**, 1640−1641.
(83) Kurniasih, I. N.; Liang, H.; Mohr, P. C.; Khot, G.; Rabe, J. P.; Mohr, A. Nile Red Dye in Aqueous Surfactant and Micellar Solution. *Langmuir* **2015**, *31*, 2639−2648.
(84) Cho, Y.; Zhang, Y.; Christensen, T.; Sagle, L. B.; Chilkoti, A.; Cremer, P. S. Effects of Hofmeister Anions on the Phase Transition Temperature of Elastin-like Polypeptides. *J. Phys. Chem. B* **2008**, *112*, 13765−13771.
(85) Abramoff, M. D.; Magalhães, P. J.; Ram, S. J. Image Processing with ImageJ. *Biophotonics International* **2004**, *11*, 36−42.
(86) Khan, V. R.; Brown, I. R. The Effect of Hyperthermia on the Induction of Cell Death in Brain, Testis, and Thymus of the Adult and Developing Rat. *Cell Stress Chaperones* **2002**, *7*, 73−90.
(87) Hume, J.; Sun, J.; Jacquet, R.; Renfrew, P. D.; Martin, J. A.; Bonneau, R.; Gilchrist, M. L.; Montclare, J. K. Engineered Coiled-Coil Protein Microfibers. *Biomacromolecules* **2014**, *15*, 3503−3510.
(88) Shrivastava, A.; Gupta, V. Methods for the Determination of Limit of Detection and Limit of Quantitation of the Analytical Methods. *Chron. Young Sci.* **2011**, *2*, 21−25.
(89) Lacey, M. E.; Subramanian, R.; Olson, D. L.; Webb, A. G.; Sweedler, J. V. High-Resolution NMR Spectroscopy of Sample Volumes from 1 NL to 10 ML. *Chem. Rev.* **1999**, *99*, 3133−3152.
(90) Currie, L. A. Detection and Quantification Limits: Origins and Historical Overview. *Anal. Chim. Acta* **1999**, *391*, 127−134.
(91) Nic, M.; Jirat, J.; Kosata, B. IUPAC Compendium of Chemical Terminology. *International Union of Pure and Applied Chemistry* **2014**, 1−1622.
(92) Wong, T. C. Micellar Systems: Nuclear Magnetic Resonance Spectroscopy. In *Encyclopedia of Surface and Colloid Science*, third ed.; Taylor & Francis, 2015; pp 4391−4409.
(93) Cheng, H. N.; Asakura, T.; English, A. D. *NMR Spectroscopy of Polymers: Innovative Strategies for Complex Macromolecules*; ACS Symposium Series; American Chemical Society: Washington, DC, 2011; Vol. *1077*, pp 3−16.
(94) Bin Na, H.; Hyeon, T. MRI Contrast Agents Based on Inorganic Nanoparticles. In *Nanoplatform-Based Molecular Imaging*; Chen, X., Ed.; John Wiley & Sons, Inc.: Hoboken, NJ, USA, 2011; pp 279−308.
(95) Schmid, F.; Höltke, C.; Parker, D.; Faber, C. Boosting (19) F MRI-SNR Efficient Detection of Paramagnetic Contrast Agents Using Ultrafast Sequences. *Magn. Reson. Med.* **2013**, *69*, 1056−1062.
(96) Robson, M. D.; Gatehouse, P. D.; Bydder, M.; Bydder, G. M. Magnetic Resonance: An Introduction to Ultrashort TE (UTE) Imaging. *J. Comput. Assist Tomogr* **2003**, *27*, 825−846.
(97) Larson, P. E. Z.; Han, M.; Krug, R.; Jakary, A.; Nelson, S. J.; Vigneron, D. B.; Henry, R. G.; McKinnon, G.; Kelley, D. A. C. Ultrashort Echo Time and Zero Echo Time MRI at 7T. *MAGMA* **2016**, *29*, 359−370.
(98) Weiger, M.; Pruessmann, K. P. MRI with Zero Echo Time. In *Encyclopedia of Magnetic Resonance*; Harris, R. K., Ed.; John Wiley & Sons, Ltd: Chichester, UK, 2007.
(99) Juchem, C.; de Graaf, R. A. B0Magnetic Field Homogeneity and Shimming for *In Vivo* Magnetic Resonance Spectroscopy. *Anal. Biochem.* **2017**, *529*, 17−29.
(100) McDaniel, J. R.; Callahan, D. J.; Chilkoti, A. Drug Delivery to Solid Tumors by Elastin-like Polypeptides. *Adv. Drug Delivery Rev.* **2010**, *62*, 1456−1467.
(101) Liu, W.; Dreher, M. R.; Furgeson, D. Y.; Peixoto, K. V.; Yuan, H.; Zalutsky, M. R.; Chilkoti, A. Tumor Accumulation, Degradation and Pharmacokinetics of Elastin-like Polypeptides in Nude Mice. *J. Controlled Release* **2006**, *116*, 170−178.
(102) Liu, W.; MacKay, J. A.; Dreher, M. R.; Chen, M.; McDaniel, J. R.; Simnick, A. J.; Callahan, D. J.; Zalutsky, M. R.; Chilkoti, A. Injectable Intratumoral Depot of Thermally Responsive Polypeptide-Radionuclide Conjugates Delays Tumor Progression in a Mouse Model. *J. Controlled Release* **2010**, *144*, 2−9.
(103) Bier, J.; Benders, P.; Wenzel, M.; Bitter, K. Kinetics of 57Co-Bleomycin in Mice after Intravenous, Subcutaneous and Intratumoral Injection. *Cancer* **1979**, *44*, 1194−1200.
(104) Tomita, T. Interstitial Chemotherapy for Brain Tumors: Review. *J. Neuro-Oncol.* **1991**, *10*, 57−74.
(105) Wang, Y.; Hu, J. K.; Krol, A.; Li, Y. P.; Li, C. Y.; Yuan, F. Systemic Dissemination of Viral Vectors during Intratumoral Injection. *Mol. Cancer Ther.* **2003**, *2*, 1233−1242.
(106) Goette, M. J.; Lanza, G. M.; Caruthers, S. D.; Wickline, S. A. Improved Quantitative (19) F MR Molecular Imaging with Flip Angle Calibration and B_1-Mapping Compensation. *J. Magn. Reson. Imaging* **2015**, *42*, 488−494.
(107) Goette, M. J.; Keupp, J.; Rahmer, J.; Lanza, G. M.; Wickline, S. A.; Caruthers, S. D. Balanced UTE-SSFP for^{19} F MR Imaging of Complex Spectra. *Magn. Reson. Med.* **2015**, *74*, 537−543.

DOI: 10.1021/acsnano.8b07481
ACS Nano 2019, 13, 2969−2985

(108) Gao, Z.-G.; Tian, L.; Hu, J.; Park, I.-S.; Bae, Y. H. Prevention of Metastasis in a 4T1Murine Breast Cancer Model by Doxorubicin Carried by Folate Conjugated PH Sensitive Polymeric Micelles. *J. Controlled Release* **2011**, *152*, 84−89.
(109) Savitzky, A.; Golay, M. J. E. Smoothing and Differentiation of Data by Simplified Least Squares Procedures. *Anal. Chem.* **1964**, *36*, 1627−1639.
(110) Pisárčik, M.; Devínsky, F.; Lacko, I. Aggregation Number of Alkanediyl-α, ω-Bis (Dimethylalkylammonium Bromide) Surfactants Determined by Static Light Scattering. *Colloids Surf., A* **2000**, *172*, 139−144.
(111) Zhang, X.; Jackson, J. K.; Burt, H. M. Determination of Surfactant Critical Micelle Concentration by a Novel Fluorescence Depolarization Technique. *J. Biochem. Biophys. Methods* **1996**, *31*, 145−150.
(112) Laginha, K. M.; Verwoert, S.; Charrois, G. J. R.; Allen, T. M. Determination of Doxorubicin Levels in Whole Tumor and Tumor Nuclei in Murine Breast Cancer Tumors. *Clin. Cancer Res.* **2005**, *11*, 6944−6949.
(113) Thao, L. Q.; Byeon, H. J.; Lee, C.; Lee, S.; Lee, E. S.; Choi, Y. W.; Choi, H.-G.; Park, E.-S.; Lee, K. C.; Youn, Y. S. Doxorubicin-Bound Albumin Nanoparticles Containing a TRAIL Protein for Targeted Treatment of Colon Cancer. *Pharm. Res.* **2016**, *33*, 615−626.
(114) Bae, S.; Ma, K.; Kim, T. H.; Lee, E. S.; Oh, K. T.; Park, E.-S.; Lee, K. C.; Youn, Y. S. Doxorubicin-Loaded Human Serum Albumin Nanoparticles Surface-Modified with TNF-Related Apoptosis-Inducing Ligand and Transferrin for Targeting Multiple Tumor Types. *Biomaterials* **2012**, *33*, 1536−1546.
(115) Soule, H. D.; Vazquez, J.; Long, A.; Albert, S.; Brennan, M. A Human Cell Line from a Pleural Effusion Derived from a Breast Carcinoma 2. *JNCI: Journal of the National Cancer Institute* **1973**, *51*, 1409−1416.

NOTE ADDED AFTER ASAP PUBLICATION

This paper published ASAP on 2/19/2019. Due to a production error, "molar residue"' was corrected to "mean residue", and the revised version was reposted on 2/20/2019.

DOI: 10.1021/acsnano.8b07481
ACS Nano 2019, 13, 2969−2985